# A Journey into Jamming: Phase Transitions and Edge-to-Edge Heterostructures in Langmuir Blodgett Films of Exfoliated Two-Dimensional Materials

by

Thomas Gregory Crabtree Storwick

A thesis

presented to the University of Waterloo

in fulfillment of the

thesis requirement for the degree of

Master of Applied Science

in

Chemical Engineering (Nanotechnology)

Waterloo, Ontario, Canada, 2024

© Thomas Gregory Crabtree Storwick 2024

## Author's Declaration

I hereby declare that I am the sole author of this thesis. This is a true copy of the thesis, including any required final revisions, as accepted by my examiners.

I understand that my thesis may be made electronically available to the public.

# Abstract

Two-dimensional (2D) materials hold significant promise as new electronic materials, and could enable high mobility devices, and flexible electronics. In particular, graphene and few-layer molybdenum disulfide have been the subject of significant study as new and exciting materials. Hindering the application of 2D materials is the lack of easy, scalable methods for deposition single layers of 2D materials. Top-down chemical methods like CVD can deposit large area high quality films, but remain highly destructive techniques, requiring high temperatures, harmful and caustic reagents, and high vacuum. Recent research in Langmuir Blodgett techniques have enabled large area coatings, continuous roll-to-roll coating, and expanded the repertoire of materials that can be coated. With this research has come renewed interest in the mechanics and dynamics of 2D materials coatings on the air-water interface. In this work, we expand this knowledge by undertaking a comprehensive study of 2D particle jamming on the air-water interface. Furthermore, we employ this understanding to demonstrate, for the first time, edge-to-edge heterostructure films assembled on the air-water interface.

To address the challenges of in-situ characterization of a growing film, we designed a method for non-destructive, in situ film monitoring using video-kymography, in addition to traditional Langmuir film characterization techniques such as surface pressure and compression isotherms.

In our findings we identify two modes of 2D material film growth on the air-water interface, an unjammed, or flowing growth mode, that is typically seen in Langmuir films of 2D materials, and a jammed growth mode, where material is condensed into a solid film by the deposition process. The key parameters that determine which mode the deposition will proceed were then identified. Within the jammed growth mode, we identify 3 phases of jammed film growth: gaseous, liquid, and solid. We then show that both the spreading dynamics of the chosen material “ink”, and the constant adding of material itself is required to progress through these stages and propose a mechanism for how a Langmuir film of 2D material can jam.

Using these findings, edge-to-edge heterostructure films of reduced graphene oxide and molybdenum disulfide were assembled on the air-water interface. Critical to the assembly of these films was the ability to deposit material in the jammed growth mode, and identify when the film was in the solid phase. This serves as a proof of concept for greater and more complex multi-material films on the air-water interface.

# Acknowledgements

I would first like to thank Dr. Pope for his mentorship, experience, and most of all, his unending patience. His advice, direction, and willingness to explore were instrumental in creating this thesis. Thank you for enduring my theories, experiments, shots-in-the-dark, and rabbit holes.

I would also like to thank the rest of the Pope research group. In particular Amanda Xu, Gillian Hawes, Elizabeth Miller, Azam Nasr Esfahani, Theeran Kanthan, and Mahshid Chekini all contributed a significant amount of their time and effort to the completion of this work, especially Amanda. The rest of you managed to make working in a lab with a constant high-pitched whine (from the glovebox blower) enjoyable. This is no small feat, and for that I will always be thankful.

I would also like to thank Dr. Nasser Mohieddin Abukhdeir and Dr. Milad Kamkar for serving on my committee. I hope this work proves interesting. I would like to thank Dr. Sean Wettig for use of his Brewster angle microscope, and Dr. Charles Dal Castel for spending 6 months repairing the atomic force microscope. I would also like to thank Dr. Xiaowu (Shirley) Tang for our collaboration, and use of her plasma cleaner.

Finally, I would like to thank my family for their support and love, and my friends for never asking about progress on my thesis. Last, but certainly not least, I would like to thank my partner Kelly Zheng for supporting me every step of the way, dealing with late night experiments, last minute schedule changes, and putting up with my inability to never leave the lab when I had planned to. You continue to be my biggest fan, strongest supporter, and best friend.

# Dedication

Dedicated to all those who helped me along the way.

# Table of Contents

Author's Declaration ..... iii

Abstract ..... iv

Acknowledgements ..... v

Dedication ..... vi

List of Figures ..... x

List of Abbreviations ..... xiii

Quote ..... xiv

Chapter 1 Introduction ..... 1

Chapter 2 Background ..... 5

2.1 2-Dimensional Materials ..... 5

2.2 Langmuir Blodgett Films ..... 5

2.2.1 Langmuir films of 2D materials ..... 8

2.2.2 Spreading Assisted Compression of Langmuir films of 2D materials ..... 9

2.3 Jamming ..... 9

2.3.1 Attractive Jamming ..... 10

2.3.2 Jamming in Interfacial Systems ..... 12

2.4 Motivation for the Project ..... 14

2.5 Outline of Thesis ..... 15

Chapter 3 Experimental Setup and Realtime In-Situ Monitoring of Langmuir-Blodgett Films ..... 16

3.1 Introduction ..... 16

3.2 Experimental ..... 16

3.2.1 Exfoliation of Molybdenum Disulfide ..... 16

3.2.2 Dispersion of Reduced Graphene Oxide ..... 17

3.2.3 Film Deposition Procedure ..... 17
3.2.4 Processing Surface Pressure Data ..... 18
3.2.5 Film Deposition Videography and Kymograph Preparation ..... 18
3.3 Surface Pressure Perturbations as an In-Situ Monitoring Method. ..... 19
3.4 Visual Characterization ..... 21
3.5 Conclusion ..... 24
Chapter 4 Jamming and Phase Transitions in Spreading Compressed Langmuir Blodget films of 2D Materials ..... 25
4.1 Introduction ..... 25
4.2 Experimental ..... 25
4.2.1 Determination of Solid Phase Material Ejection Speed ..... 25
4.2.2 Brewster Angle Microscopy ..... 25
4.2.3 Langmuir Areal Concentration ..... 26
4.2.4 Spreading force dissipation distance ..... 26
4.2.5 Particle Tracing using TrackPy ..... 26
4.3 Jammed and Flowing Films ..... 27
4.4 The Phases of Jammed Film Growth ..... 30
4.5 Investigating the Conditions that Cause Jamming ..... 32
4.6 Probing the Mechanism of the Jamming Transition ..... 35
4.7 Conclusion ..... 42
Chapter 5 Printing Edge-to-Edge, Lateral Heterostructures on Water ..... 44
5.1 Introduction ..... 44
5.2 Experimental ..... 44
5.3 Printing Lateral Heterostructures ..... 44

Chapter 6 Conclusion and Future Work ..... 47
6.1 Summary of Findings ..... 47
6.2 Recommendations for Future Work ..... 48
6.2.1 Fluid Dynamic Analysis of the Spreading Front ..... 48
6.2.2 Additional Heterostructure Materials ..... 48
6.2.3 Heterostructure Based Electronic Devices on the Air-Water Interface ..... 48
References ..... 50

# List of Figures

Figure 1: Schematic diagram of a Langmuir-Blodgett trough, reproduced from [24]. ..... 7
Figure 2: Example Langmuir compression isotherm for $MoS_2$ nanosheets. Reproduced from [25]..... 8
Figure 3: The jamming phase diagram proposed by Liu and Nagel. Reproduced from [31]. ..... 10
Figure 4: Examples of particle systems with both weak and strong attraction (*a*), at various packing fractions (ϕc). Red particles indicate the largest percolating structure. Note the sharp transition in percolation, and rigidity, for the weakly attracting system versus a more gradual transition for the strongly attracting case. Reproduced from [32]. ..... 11
Figure 5: Proposed jamming phase diagram for attractive systems. kbTU is a dimensionless representation of the temperature relative to the interparticle attractive energy U, σσ0 is a dimensionless representation of stress in the system, and 1ϕ is the particle packing fraction. Reproduced from [31]. ..... 12
Figure 6: (Top) Surface pressure vs area isotherm for a monolayer of 1 μm silica spheres deposited on the air-water interface. (Bottom) Root mean square (RMS) amplitude of surface pressure oscillations due to the stepper motor's mechanical force oscillations. Reproduced from [37] ..... 20
Figure 7: (Left) Surface pressure over time for an $MoS_2$ deposition. The width of the signal is due to repeated spikes in surface pressure from additional droplets being added to the surface. (Right) Root mean square (RMS) amplitude of the signal on the left. ..... 21
Figure 8: (Left) Image of a reduced graphene oxide (rGO) film in the free-flowing state, and (right) image of the same film after it has solidified into the rigid state. Note the eddies present at the film edge in the free-flowing state. Scale bars are 1cm. ..... 22
Figure 9: Diagram showing the processing making a kymograph. The vertical yellow line in the (a) corresponds to the vertical array of pixels. (b) Shows a depiction of the process acting on every frame of the video, resulting in (c), a diagram showing each pixel array being arranged sequentially. (d) The final kymograph image. ..... 23
Figure 10: Still images from the deposition of $MoS_2$ Langmuir films have either a) not jammed and remained flowing throughout the deposition, or b), jammed and became rigid during deposition. A) and b) show still images of the film deposition before, during, and after a material ink droplet spreads on the surface. Scale bar is 1cm. C and d) show the resulting kymographs for the flowing and jammed films respectively. Scale bar is 20s. As the MoS2 film is somewhat transparent, the top and bottom image sets' brightness and contrast have been heavily edited for clarity. ..... 28

Figure 11: Pixel grey values for both jammed and flowing films of $MoS_2$. A darker pixel corresponds to a lower grey value. ..... 29
Figure 12: Stages of film deposition for a jammed film of $MoS_2$ showing the a) gaseous, b) liquid and c) solid phases. Brightness and contrast have been heavily edited for clarity. ..... 30
Figure 13: Compression isotherm of a jammed rGO film. The "kink" at approximately (6000, 39) indicates monolayer collapse and the maximum film compression [25]. ..... 31
Figure 14: Kymograph of a jamming MoS2 film deposition. Gaseous, liquid, and solid phases, as well as the deforming film edge are indicated. Scale bar is 20s. ..... 32
Figure 15: a) A phase diagram indicating the conditions under which the nanomaterial film will jam under deposition. The y axis corresponds to the Langmuir areal concentration, the areal concentration of the solution as measured by a Langmuir trough. The x axis corresponds to the distance from the barrier where the spreading force from the ink droplet dissipates. Square, triangle, and circle markers correspond to rGO in butanol/DCE, rGO in ethanol/DCE, and $MoS_2$ in DMF/DCE respectively. b) Scanning electron microscope images of rGO films deposited at various concentrations and spreading dispersants. White numbers indicate the packing fraction of the film obtained by image thresholding from N=5 different images of the film at different magnifications and areas. Scale bar is 10 μm in all images. Films in b).i-iii used ethanol as the spreading dispersant with an area concentration of 472 $mm^2$/ml, 944 $mm^2$/ml, and 9442 $mm^2$/ml respectively. Films in c).i-iii used butanol as the spreading dispersant at an areal concentration of 236 $mm^2$/ml, 472 $mm^2$/ml, and 9442 $mm^2$/ml respectively. ..... 33
Figure 16: A kymograph of rGO deposition where the ink was switched to a pure dispersant mixture before the liquid state was reached, which we hypothesized would condense the film without the addition of material. Instead, the material remained in the gas phase. b) Kymograph of a typical rGO deposition for comparison with a), showing the transition to a liquid and subsequently solid phase film at the right side of the image. c) Kymograph of a liquid phase rGO film being subjected to the dripping of an ink composition with only dispersant, no nanomaterial, showing the ablated material from the film edge. d) Kymograph of ablated liquid film from c) resolidifying after a return to a rGO suspension as the deposition ink. ..... 36
Figure 17: a) Image sequence of an rGO deposition showing the dispersant spreading front. b) Image of an $MoS_2$ film deposition showing particles on the surface. Scale bar is 1cm c) Particle traces of the movement of the particles in b) after the spreading front had dissipated, generated using TrackPy over a period of 3s. Scale bar is 1cm. ..... 38

Figure 18: Brewster angle microscopy images showing the microstructure of growing films of $MoS_2$ in both a) the flowing growth mode, and b) the jamming growth mode. c) Elastic modulus under compression for both a jamming and unjammed film of $MoS_2$, inset shows the original compression isotherm using Π to denote the surface pressure. ..... 40
Figure 19: Heterostructure interfacial films of 2D materials. a) A heterostructure film of rGO and $MoS_2$, showing the two films and the contact line between them. Scale bar is 1cm. b) The film in a) just after rGO deposition i), after the interface is cleaned with surface aspiration ii), the ablated interface caused by the deposition of $MoS_2$ iii), and a zoomed in photo of that interface iv). The scale bar in b. i), ii), and iii) is 1 cm. The scale bar in b. iv) is 5 mm. c) A heterostructure film of rGO and $MoS_2$, where the $MoS_2$ was deposited first. d-f) SEM images of the film in a), showing the interface between rGO and $MoS_2$, after the film was deposited on a section of Si wafer. ..... 45

## List of Abbreviations

| | |
|---|---|
| 2D | two-dimensional |
| $MoS_2$ | molybdenum disulphide |
| hBN | hexagonal-boron nitride |
| AM | additive manufacturing |
| LB | Langmuir-Blodgett |
| 2DLB | Two-dimensional Langmuir-Blodgett |
| RMS | Root Mean Square |
| rGO | Reduced Graphene Oxide |
| DCE | 1,2-dichloroethane |
| DMF | dimethylformamide |

Time is money.

If you’re done shopping, then quit wasting both.

# Chapter 1
# Introduction

The demands of modern electronics continually push the limits of materials development. Continuing to propagate Moore's law means not only developing new fabrication techniques, but also materials with electronic properties to suit the unique challenges of developing these tiny electronic devices. Similarly, flexible electronics, advanced displays, smart clothing, implantable devices, and advanced solar cells all require new materials to meet the constraints of these new applications. To meet these challenges, one class of material has received significant attention in the last decade: Single layer or few layer two-dimensional (2D) materials.

2D materials are comprised of a few atomic layers of constituent elements, usually where the in-plane bonds are stronger than those between the basal planes. Since their original discovery by Geim and Novoselov with their isolate of graphene from bulk graphite, a wide range of atomically thin 2D materials have been discovered whose properties often differ greatly from those of the bulk material [1]. Most notably graphene, molybdenum disulphide ($MoS_2$), and hexagonal-boron nitride (hBN) have been used to great effect towards the development of next generation electronics. The combination of a high mobility conductor: graphene, a direct band-gap semiconductor: 1T-$MoS_2$, and a highly stable insulator: hBN, has enabled the construction of junct0069on based devices made of only a few atomic layers [2], [3], as well as the advancement of existing devices modified with these materials. Outside of electronics, 2D materials have shown their ability to provide efficient gas filtration [4], form strong composites [5], and provide stable hydrophobic coatings [6].

In almost all these applications the first steps to use the material are, rather naturally, to make the material and deposit it on a substrate. In the case of 2D materials, production usually falls into two categories: nanofabrication methods and solution exfoliation methods. Nanofabrication methods like chemical vapor deposition provide high quality and low defect films, sometimes even over large areas. However, expensive machinery, long processing times, and harsh deposition conditions often mean these are more suited for highly sensitive, low volume applications. On the other hand, in solution exfoliation methods, the bulk material is separated into its constituent layers. Examples such as chemical exfoliation [7] electrochemical exfoliation [8], or shear-induced exfoliation in suitable dispersants [9], can offer a lower film quality; however, these methods offer a much easier path to

scale, being inherently lower-cost, less equipment intensive, and offer more flexibility in processing as there are no substrate requirements and the exfoliation processes are often carried out under ambient conditions making them suitable for future flexible and wearable electronics. While each method has its own merits, in all cases, the resulting dispersions can be formulated into thin films or formulated into inks for printing.

Regardless of the exfoliation method, all solution-based inks must be printed onto a substate. Various typical printing methods exist to create patterns and coatings from 2D material inks, most notably as tape casting, inkjet printing, gravure, slot-die, etc. Since the thickness of single layers for most 2D materials is ~1 nm, and the thinnest film obtainable by these methods is usually 1 μm, these films are composed of hundreds to thousands of restacked sheets. This restacking somewhat defeats the purpose of initially separating the material into monolayers. On the other hand, a few methods exist that are capable of depositing uniform films at the nanometer thickness scale such as the use of rod-coating and Langmuir-Blodgett related approaches [10], [11]. In particular, the Langmuir-Blodgett methods offers the possibility of retaining the attributes of single layers such as flexibility, transparency, and thickness-related optoelectronic properties [12]. Originally developed for lipids and surfactants, Langmuir-Blodgett films are made by suspending the material of interest at the air-water interface. The material is then deposited by dipping the substrate through the interface (Langmuir Blodgett deposition), or by lowering the water (subphase) past an originally submerged substrate (horizontal precipitation method).

Recent advances have taken the Langmuir-Blodgett method from a batch process to a continuous one [11], [13]. By leveraging either the flow of the subphase water or the spreading dynamics of nanomaterial dispersions, the surface material can be condensed into a uniform film and transferred to a continuously fed substrate. These advances help move Langmuir Blodgett films from the lab into an industrially relevant, potentially scalable, large area nanomaterial deposition technique. Repeated depositions can add layers, building up films in a manner like additive manufacturing (AM), opening the possibility for devices of consisting of multiple deposited layers of nanomaterials. However, unlike AM where it is common to print patterns of multiple materials within one layer, until now there has been no progress of creating Langmuir films consisting of two or more distinct regions of material.

This is likely due to the dynamics of depositing nanomaterials onto the air-water interface. In AM, printed material is almost always solid shortly after leaving the printing-zone, providing limited opportunity to mix between materials. By contrast, nanomaterials frequently move and diffuse on the air-water interface. Compounding this, high aspect-ratio nanomaterials are often dispersed in dilute solutions to prevent aggregation due to their low mechanical percolation thresholds [14]. When dispersing these materials on the air-water interface, often millilitres of solution are added dropwise to deposit sufficient material, in contrast to the 1-2 drops (few hundred microliters) of concentrated lipid solutions [15]. This repeated dripping onto the interface provides constant mechanical mixing, preventing the separation of different materials. If patterning is possible, the material must be made into a solid-like film that could resist this mixing.

A similar problem is found when making a continuous, roll-to-roll, deposition setup. To deposit a dense and solid film onto the rolling substrate, a dense and solid film must first be formed on the air-water interface. If the material is allowed to float freely on the interface, the deposited film will be patchy, and non-unform. Instead, the floating material on the surface must be gathered and compressed into an unbroken film and pushed onto the fed substrate. For roll-to-roll processes, new research has leveraged the force created from the spreading of the nanomaterial dispersion on the subphase water to apply this compression in a roll-to-roll system [11]. We have also used it to create highly dense tiled films of 2D flakes such as graphene oxide (GO), molybdenum disulphide ($MoS_2$) [16], and hexagonal-boron nitride [17].

In our method we have observed that more than just a gathering of material is required, the film must be compressed until it is jammed into a rigid state for the force from the spreading droplet to push the film uniformly onto the substrate [11]. Our group has furthermore observed this jamming with multiple materials different sizes, functional groups, and surface charges. This suggests that that the film behavior is not dominated by a specific particle-particle interaction, but instead comes from the dynamics of packed 2D sheets on the interface.

With the importance of jammed films for both continuous deposition and patterning, attention should be paid to how and why films of 2D nanomaterials jam on the air-water interface, and its applications. The main objective of this work is to use jammed nanomaterial films to create edge-to-edge heterostructures entirely on the interface. This will lead to better understand the process dynamics of spreading-compressed Langmuir Blodgett films, leading to higher quality films in the

future, and provides a demonstration of this control by forming multi-material films. To reach this goal, 3 steps are required. Firstly, a method of in-situ monitoring of the film dynamics and its rigidity. Secondly, an investigation into the mechanics of jamming of 2D materials on the air-water interface during a spreading-compressed Langmuir-Blodget deposition. Finally, applying the results of the investigation in the formation of two distinct regions of different materials joined by an edge-to-edge heterostructure on the air-water interface. Specifically, this thesis will present:

1. A method to monitor the film rigidity in-situ. This enables the ability to track the films progress in a non-destructive way.
2. An analysis of the jamming points and phase transitions in spreading-compressed Langmuir Blodget films.
3. A demonstration of multi-material films joined by edge-to-edge heterostructures, showing how the understanding of film rigidity and jamming can lead to better control over film formation.

# Chapter 2
# Background

## 2.1 2-Dimensional Materials

2D materials are a class of material defined by geometry, having one dimension that is extremely thin, and the other two being roughly on the same order and being much larger than the thickness [18]. Usually, and for the purposes of this thesis, they are isolated from materials that have strong and usually covalent in-plane bonding, but weak or van der Waals bonding between the atomically thin planes. This weak bonding allows for the planes to be isolated into individual sheets consisting of often only a single or few layers of atoms. As mentioned in the introduction, there are many precursor based methods for creating high quality material. These methods, like chemical vapor deposition, pulse laser-deposition, metal–organic chemical vapor deposition, have their advantages, but have limits to their scalability [18].

Instead, the methods used in this thesis are exfoliative methods. These methods begin with a layered crystal and strip off individual layers. While there are many ways of doing this, two of the most common, and used here, are ultrasonication and chemical exfoliation. In chemical exfoliation, a highly reactive reagent is used that interweaves itself between the layers of the crystal, and then the intercalated crystal is placed in a second reagent reacting with the first (e.g., the intercalated lithium compound and water) [16]. This reaction generates gas between the crystal planes, and the force of this gas evolution separates the individual sheets of the crystal. The second method, liquid exfoliation (e.g., ultrasonication), uses high shear or high energy mixing applied to a dispersion of the bulk crystal to mechanically cleave the layers apart [18]. Ultrasonication, the method used in this thesis, is proposed to work via cavitation, where small bubbles caused by the ultrasonic generation expand and break off sheets of material [19].

In either case, after exfoliation the resulting solution is a dispersion of few or single layer nanosheets suspended in the dispersant of choice.

## 2.2 Langmuir Blodgett Films

Langmuir films have a long and storied history that has been covered by many theses, and readers interested can find more in reference [20]. They are, typically, monolayer films of lipids or

surfactants that are suspended at the air-water interface. While none of this work deals with the monolayer suspension of lipids or surfactants, in fact great care was taken to avoid the presence of these species, the mechanics behind lipid film suspension are very similar to flakes of 2D materials [21].

Langmuir films are typically formed by adding a small drop of surfactant or insoluble amphiphile to an existing, clean air-water interface. As the surfactant is added, it spreads on the surface, and as it does so it changes the air-water interface to an air-surfactant-water interface. The energy for the air-water system is given by equation **1**$E_0 = \gamma_{aw}$, and the air-surfactant-water system by **2**:

$$E_0 = \gamma_{aw}, \quad \mathbf{1}$$

$$E_L = \gamma_{as} + \gamma_{sw}, \quad \mathbf{2}$$

where $\gamma_{aw}, \gamma_{as}, \gamma_{sw}$ are the surface energy of the air-water interface, the air surfactant interface, and the surfactant water interface, respectively. A Langmuir film will be stable if the energy of the air-surfactant-water system is less than that of the air-water system, that is: $E_L < E_0$. Since $\gamma_{aw}$ is very large, 72.8 $\frac{mJ}{m^2}$ at room temperature, stable Langmuir films are possible with many materials [21], [22]. This analysis also provides insight into why only a monolayer is formed, as additional layers make no difference to the interfacial energy and therefore extra surfactant often remains solubilized in the water phase. One measure of film stability is the surface pressure Π which equal to the difference in energy between the two states [23].

$$\Pi = E_0 - E_L = \gamma_{aw} - \gamma, \quad \mathbf{3}$$

The energy of the second state is usually measured experimentally by Wilhelmy plate or similar method and therefore is denoted by $\gamma$ here. A small Π can mean that either the surfactant being used has little effect on the total interfacial energy, or more likely that there is not enough insoluble amphiphile to entirely cover the interface. In these situations, incrementally compressing the interfacial area (without changing the total amount of surfactant) will increase the surface pressure as the interfacial concentration increases [21]. This area is changed by placing 2 barriers across the interface that partially submerged. In this way, they fully confine the surface, but do not touch the bottom of the container, meaning bulk water can move freely from to and from either side of the barrier. To reduce the interfacial area, the barriers are moved closer together. The mechanism to do this is shown in Figure 1.

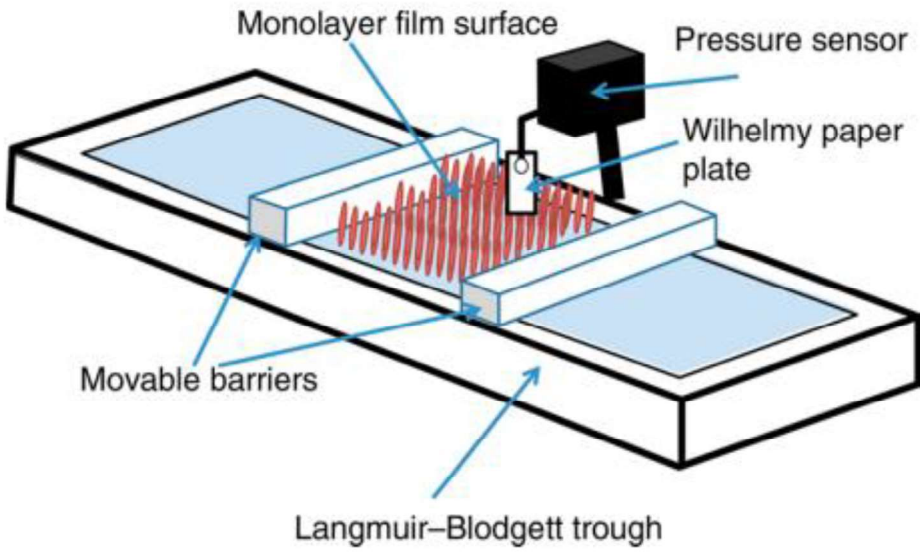



**Figure 1:** Schematic diagram of a Langmuir-Blodgett trough, reproduced from [24].

This works up to a point. Once the interface is fully saturated, further compression cannot increase the interfacial concentration. Instead, continuing to compress the film causes one of two things to happen. If the added compound is a surfactant, the surface pressure will plateau as continued pressure causes the surface to form micelles and equilibrate into the bulk. Instead, if the added compound is an insoluble amphiphile, continued barrier compression causes the monolayer film to buckle and collapse, resulting in a sharp drop in surface pressure [21]. This second case is the one relevant to this thesis. Plotting the surface pressure against the interfacial area results in the Langmuir compression isotherm (Figure 2). In this isotherm, 3 phases are normally identified: the gaseous phase, denoted by I in the figure, the liquid phase, denoted by II and III in the figure, and the solid phase, denoted by IV in the figure. In the gaseous phase, particles float freely on the surface, making little change to the overall surface pressure. In the liquid phase, particles begin to interact regularly, slowly increasing the surface pressure; however, there is still significant free interface. Finally in the solid phase particles are forced together and most of the remaining free interface is filled. Here, the film has elastic-like properties rather than viscous ones, and the film is so tightly packed that it is common to use this final area, in combination with the amount of material deposited, to estimate the size of molecules [12]. The area denoted by V denotes monolayer collapse, and bucking of the interfacial layer.

Since the above is measuring the compression of a film and its physical response, an elastic modulus for the film can be defined by equation **4**, where $E$ is the elastic modulus of the film, $A$ is the area of the film, and $\frac{d\Pi}{dA}$ is the derivative of the surface pressure $\Pi$ with respect to the film area $A$.

$$\boldsymbol{E = -A\frac{d\Pi}{dA},} \qquad 4$$

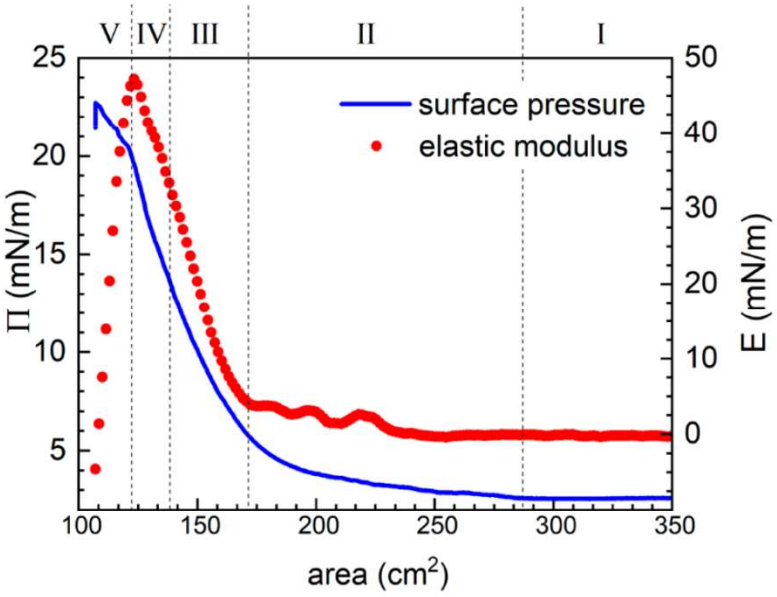



**Figure 2:** Example Langmuir compression isotherm for $MoS_2$ nanosheets. Reproduced from [25].

### 2.2.1 Langmuir films of 2D materials

As mentioned in the introduction, Langmuir films of 2D materials require much more volume than the one or two drops of concentrated lipids to fill the interface in the traditional approach. Due to mechanical percolation thresholds of large aspect ratio nanomaterials [16], dispersions cannot be made that have a high enough concentration. This means that Langmuir films of 2D materials need to be formed over many drops. This induces both mechanical perturbation and excess dispersant into the Langmuir system compared to the lipid case.

Care must also be taken when determining the dispersants used in the process. To help the nanomaterial to remain on the surface the dispersing solution is usually hydrophobic [21]. However, examples using hydrophilic dispersants exist. Finally, to avoid material aggregation as the droplet

dries, the solution should spread readily on the air-water interface, dispersing the individual material sheets on that interface.

### 2.2.2 Spreading Assisted Compression of Langmuir films of 2D materials

Recently, barrier free compression of a nanomaterial film on the air-water interface has been achieved by leveraging the spreading force created by the material dispersion [11], [15]. Since films deposited in this barrier free manner for the basis of study for this thesis, a brief overview of their formation is given here. During a spreading compressed film deposition, a material ink is chosen that not only suspends the nanomaterial for enough time to complete the deposition, but also so that the dispersant mixture spreads readily on the surface. This material ink is dripped dropwise onto the air-water interface. As the droplets hit the surface, they spread out, forcing the material to the edge of the trough. After spreading, the remaining dispersant then either evaporates or dissolves into the subphase water. Repeating this process causes more and more material to build up at the edge of the Langmuir Blodgett trough.

## 2.3 Jamming

Jammed systems are encountered everyday. For example, the traffic jam, dry powders jammed in a factory hopper, and the jammed atoms in a glass material [26]. All these systems are characterized by a transition from a flowing state to a rigid one without a change in order, called the jamming transition. The field of jammed materials was originally studied with ground-breaking work by Cates et al. [27], and Liu and Nagel [28], which characterized the field using analysis based on frictionless, a-thermal, hard spheres. They discovered that jammed systems have similar properties: the material is disordered, the material structure looks similar before and after jamming, and that the transition to rigidity is usually governed by the temperature, packing fraction, and applied stress. Liu and Nagel codify these three properties into a jamming phase diagram able to characterize a jammed vs. unjammed state (Figure 3) [29]. O'Hern et al. show the particle-level reasons for these transitions: A system is mechanically stable (in the a-thermal, non-attractive, frictionless state), if a particular particle is held in place by more neighbors than 2d, where d is the number of dimensions in the system (2 for circles, 3 for spheres, etc.)[30]. For those neighbors to hold the original particle in place, they must be rigid, and therefore also be held in place by greater than 2d neighbors, who in turn

must be held in place by greater than 2d neighbors, and so forth. Therefore, to go from a flowing to rigid material, rigidity must rapidly percolate throughout the system at some finite point, resulting in the jamming transition [30]. Jammed systems therefore have a sharply defined transition point stemming from increasing packing fraction at 0 K and no applied strain, and this point is referred to as point J [29].

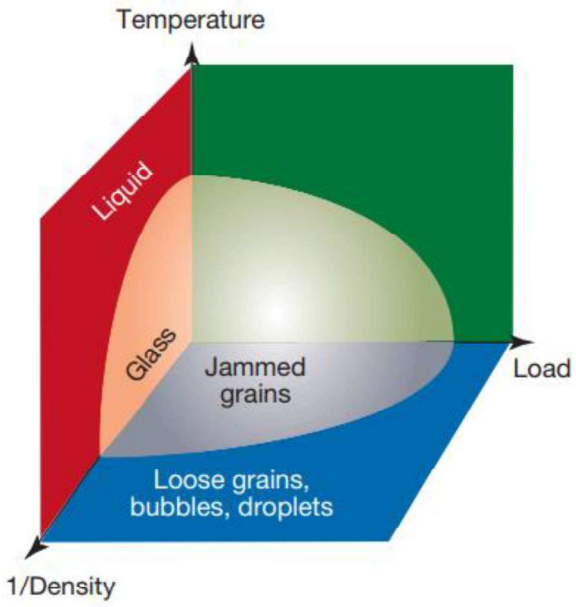



**Figure 3:** The jamming phase diagram proposed by Liu and Nagel. Reproduced from [31].

### 2.3.1 Attractive Jamming

More recent advances have begun to look at jamming between attractive particles, which can provide a useful background for understanding jamming in interfacial films of 2D materials. In particular, Koeze and Tighe show that jamming between attractive particles is quite different than non-attractive and forms a new type of jamming [32]. Critically, they show that in the infinite particle limit, any amount of attraction between particles moves the system to the attractive jamming regime, even for small attractive forces, and that increasing attraction between particles lowers the critical packing fraction required for jamming and smooths the transition itself. Furthermore, they show that attractive jammed systems have percolating clusters that can span the length of the system, but do not encompass all or almost all of the particles in that system (Figure 4). This contrasts with the

dimensionality argument made for unattractive jammed systems, where all particles in the system need to support each other for a system to become rigid. This results in the smoothing of a once sharp transition. Weitz et al. use these arguments to propose a modified jamming phase diagram for attractive colloidal particles [31].

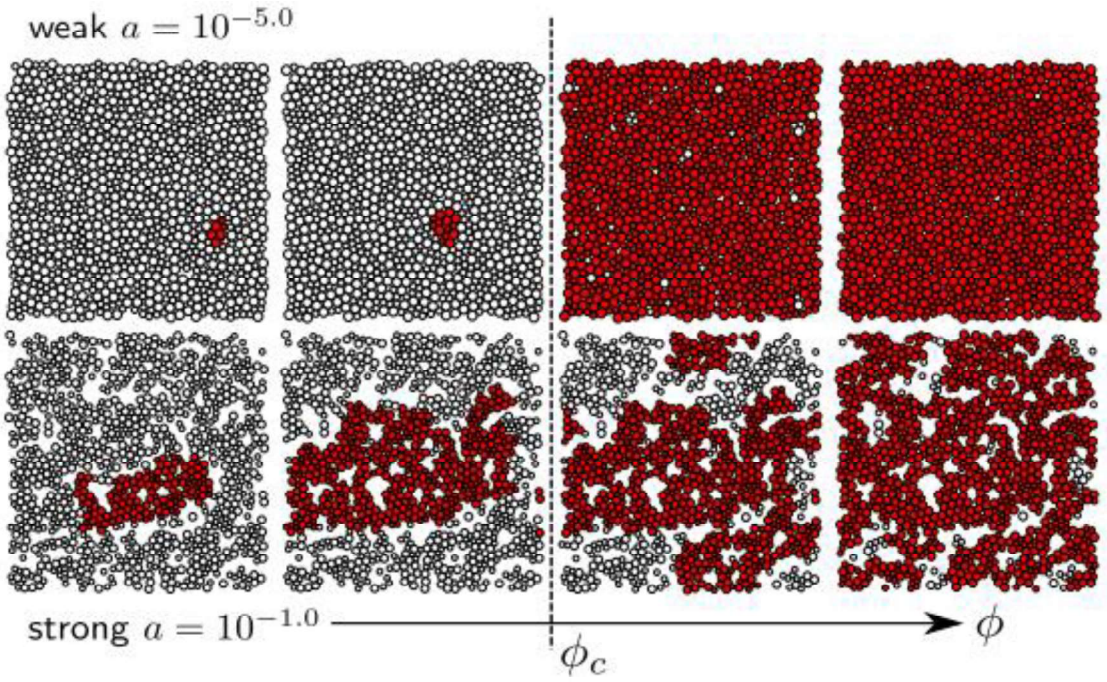



**Figure 4:** Examples of particle systems with both weak and strong attraction ($a$), at various packing fractions ($\boldsymbol{\phi_c}$). Red particles indicate the largest percolating structure. Note the sharp transition in percolation, and rigidity, for the weakly attracting system versus a more gradual transition for the strongly attracting case. Reproduced from [32].

Zheng et al. expand on the class of jammed attractive materials by examining the effect of shear flows on attractive jamming systems. They show that these systems can be induced to rigidity by small shear flows, at packing fractions well below the threshold for jamming, and then the same systems can be broken up by larger shear stresses. Zheng et al. also show the existence of shear gel phases, formed of low density, semi rigid particles at very low shear stresses. Analysis by Lois et al.

show that these shear-induced clusters are only rigid one way, i.e. clusters that were induced by shear flows can be undone by a shear flow in the opposite direction.

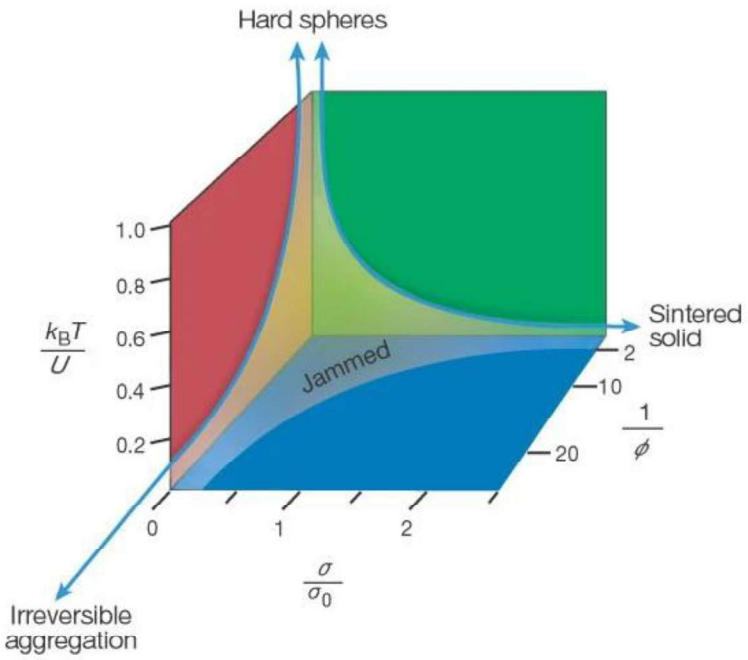



**Figure 5:** Proposed jamming phase diagram for attractive systems. $\frac{k_b T}{U}$ is a dimensionless representation of the temperature relative to the interparticle attractive energy $\boldsymbol{U}$, $\frac{\sigma}{\sigma_0}$ is a dimensionless representation of stress in the system, and $\frac{1}{\phi}$ is the particle packing fraction. Reproduced from [31].

### 2.3.2 Jamming in Interfacial Systems

Recently, there has been much interest in using the mechanics of jamming to explain and predict the behavior of interfacial films. One of the systems most often looked at are colloidal particles, which, despite having finite interactions, non-zero temperatures, and other properties that violate the simple model assumptions, often still act similar to this model case. Chai et al., provide a direct observation of this effect using in-situ AFM to probe the effects of particle jamming, showing the solid-like effects of a highly packed layer [33]. Without an AFM, interfacial viscoelastic properties are usually measured using the surface pressure under compression, using the Gibbs isotherm and the relation:

where $E$ is the elastic modulus, $A$ the area, and $\Pi$ the surface pressure. These properties can also be measured by an interfacial rheometer [34]. The jamming and viscoelastic properties of surface films can be highly influenced by the particle-particle interactions between them, and whether they can be considered negligible in the system. The attractive force in colloidal systems is often the van der Waals force, which Williams and Berg have extended to interfacial particles [35]. These van der Waals forces are often stabilized by a repulsive electrostatic force for charged particles. A force unique to the interface is the capillary forces at the interface. Large, heavy particles can deform the interface under their weight, and can attract or repel other particles with this interface deformation.

These forces are well-established for bulk (i.e., 3d) colloidal systems, and significant success has been found in adapting these theories to colloidal particles trapped at an interface. In the context of 2D materials, however, many of these interactions are unclear. Dispersions of 2D materials almost always contain a larger distribution of particle sizes and shapes, making it difficult to define a typical particle-particle interaction. Furthermore, the atomically thin nature of 2D materials presents a challenge when quantifying these interactions. For example, it is difficult to define the fraction material immersed in the liquid phase when it has the same thickness as this interface.

## 2.4 Kymographs and Videokymography.

Kymographs and kymography are used frequently throughout this thesis. Originally used to measure blood pressure, the technique is a way to visualize highly dynamic systems, revealing patterns in the time evolution of that system [36]. More recently, and perhaps more interestingly, the technique has expanded as a video processing technique called videokymography. It was originally invented by Jan G. Švec to visualize the high-speed vibrations of vocal chords [37]. In this technique, a video is taken of the of the subject, in Švec et. al's case the vocal folds, and then from each frame of the video a single line of pixels is taken (Figure 6). These single lines of pixels are then composited side by side into an image, where one direction in the image is a spatial axis from the original video, and the other is direction displays changes in time. In this way, a videokymograph can be used to represent an entire video in a still image, assisting in analysing how the filmed subject changes in time.

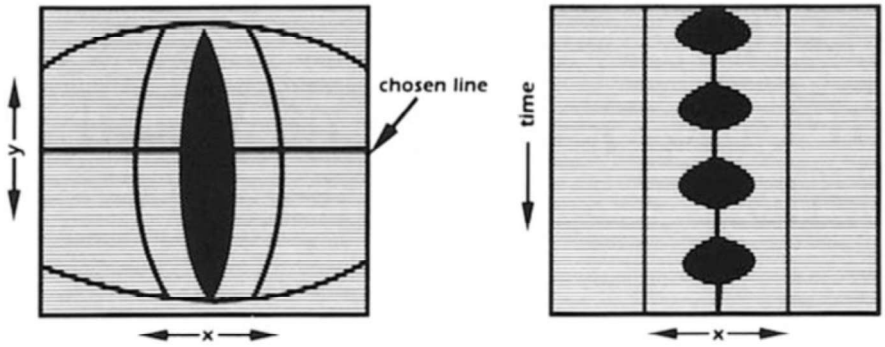



**Figure 6:** Diagram showing the construction of a videokymograph from a video of human vocal folds. Note how in the second image the vertical axis now displays time. Reproduced from [37]

## 2.5 Motivation for the Project

Significant previous work has been done on Langmuir Blodgett films of 2D materials. Specifically, spreading assisted, barrier free, films have been demonstrated with many materials, and more interestingly a continuous roll-to-roll version has been demonstrated [11], [16], [17]. This progress has uncovered several open questions about the film formation: Is it required to have a rigid film on the surface for the roll-to-roll process as the spreading pressure of each droplet pushes against the leading edge of the film and provides a force to transfer the film onto the substrate? Through trial and error, specific ink recipes have been discovered that work to create this phase, while other recipes do not. An investigation into what it means to have a rigid film, why a film transitions into a rigid phase, and what determines the ink formulation that can give a successful deposition has not been explored until now. Furthermore, this thesis will be the first exploration into the methods by which the film initially forms.

Secondly, and perhaps more interesting, is the possibility of multi-material films and edge-to-edge heterostructures formed on the air-water interface. Langmuir Blodgett deposition is continuing to show its applicability for scalable deposition of large area nanomaterial films[11], [16]. Creating films of multiple materials demonstrates an advanced level of control over film formation. Multi-material films also opens the possibility for edge-to-edge heterostructure devices to be created entirely using the Langmuir Blodget technique, rather than post processing techniques of stamp-transfer or masking and performing a second deposition. Finally, this is the first step in a long journey to creating complex structures on the surface of water, perhaps even with the level of control as an

inkjet printer, allowing for complex electronics and nanomaterial devices to be created using one deposition step; a deposition step that can use almost any substrate, and operates at room temperature.

## 2.6 Outline of Thesis

The main goal of this thesis is to construct edge-to-edge heterostructure films on the air-water interface, and to investigate the conditions necessary for those films to be made. This thesis contains three main sections of work that was done in pursuit of this goal: the development of an in-suit characterization technique, analysis of the film growth, and a demonstration of edge-to-edge heterostructure films on the air-water interface.

Chapter 3 details the development of a in-situ non-destructive measurement technique used to monitor and analyze the films as they are growing. It shows how videography was used to characterise the films, and how this videography could be translated into easily digestible kymograph images. This informs much of the analysis in chapter 4.

In chapter 4, the two modes film growth are described, jammed, and not jammed/flowing. It is shown how the conditions of the deposition setup, principally the nanomaterial ink composition and concentration, determine under which mode the deposition will proceed. Within the jammed growth mode, 3 phases of film growth were identified: gaseous, liquid, and solid. It is shown that the transitions between these states are abrupt, and that both the spreading of subsequent droplets, and the addition of material is required to transition between states. A mechanism for how the film jams is also proposed.

Finally, chapter 5 shows the culmination of the understanding gained in chapter 4. By depositing films that are not only jammed, but also in the solid phase of jammed growth, edge-to-edge heterostructure films on the air-water interface are demonstrated. Remarkably, these films show very little mixing between the two materials and serve as a proof of concept for future work.

# Chapter 3
# Experimental Setup and Realtime In-Situ Monitoring of Langmuir-Blodgett Films

## 3.1 Introduction

As mentioned in chapters 1 and 2, an overarching theme of this work is to investigate jamming in LB films of 2D materials. Previous work on LB films in the Pope group has required a rigid film for various applications, including the aforementioned roll-to-roll system. In these cases, the presence of a rigid and continuous film has been confirmed visually by the experimenter, through a series of clues including: does the film deform when further ink-dispersion droplets are applied to the surface, is the film "dark enough", and will the film hold its shape when the addition of further dispersion is stopped? These clues, while sufficient for an early investigation into the dynamics of this system, and can be helpful for experiment setup, are not rigorous enough for an investigation into jamming in this system. Therefore, the first step taken to investigate jamming in two-dimensional Langmuir Blodgett (2DLB) films is a repeatable film characterization method.

Since we are investigating a film during its formation, spontaneous changes the films undergo are important. For this reason, an in-situ measurement technique that has minimal effect on the film's formation itself is required. A second but important consideration long suspected in the 2DLB community is that a film on the surface may undergo some transformation from being suspended in the interface, to deposited on a substrate. The extent of this transformation, and its significance on the final film morphology remains to be determined. In order to ensure that this work remains as relevant as possible depending on substrate type and deposition method, an in-situ measurement technique is preferred.

## 3.2 Experimental

### 3.2.1 Exfoliation of Molybdenum Disulfide

$MoS_2$ was exfoliated in the method described by Chen et al, a modified version of Eda's method [38]. Briefly, 0.5 g of $MoS_2$ powder (SigmaAldrich, ~6 μm) was mixed with 7 mL of 1.6 M n-butyllithium solution in hexane (Sigma-Aldrich) in a 25 mL reaction vessel. It was then placed for in an Ar-filled glovebox (O2 and H2O < 1 ppm) for 3 days, under continuous stirring. This step is to intercalate bulk

$MoS_2$ crystal with lithium. The intercalated $MoS_2$ was then filtered into a filter cake, washed with 80 mL of hexane to remove excess n-butyllithium, and then placed into a large beaker containing 150 mL of deionized water to chemically exfoliate the $MoS_2$. A visible reaction should be observed at the point of introduction. The beaker and solution were then bath sonicated (TruSonik, 2.5 L, 120 W) for 1 h to complete the exfoliation process. Following sonication, the dispersion was then re-filtered into a filter cake, and dispersed into 150 ml of N,N-Dimethylformamide (DMF) as a dispersant exchange. The solution was then re-sonicated for 1 h using bath sonication to ensure redispersion. Finally, the MoS2 in DMF was centrifuged at 3500 rpm for 1 h to remove unexfoliated MoS2 using a Fisher Scientific AccuSpin 3. The supernatant was then transferred to 50ml centrifuge tubes, covered from light, and stored for use. All solutions were used within 2 weeks of exfoliation to limit material degradation.

For preparation of $MoS_2$ inks for deposition. $MoS_2$/DMF solution was mixed in a 3:1 $MoS_2$/DMF:DCE ratio by weight.

### 3.2.2 Dispersion of Reduced Graphene Oxide

5mg of commercially available reduced graphene oxide (rGO) powder (Global Graphene Group, Gi-PW-B050) was added to 10 mL of 1,2-Dichloroethane (DCE). The mixture was then probe sonicated for 2 hours (60% amplitude, Model 150VT Ultrasonic Homogenizer, BioLogics Inc.; Sonics Vibra-Cell VCX-500 Ultrasonic Processor, Sonics & Materials, Inc.) submerged in an ice bath to prevent overheating. The dispersion was then transferred into a glass centrifuge tube and centrifuged (AccuSpinTM 3, Fisher Scientific, Waltham, MA) at 500 RPM for 30 min to remove undispersed particulates.

For preparation of rGO inks for deposition. rGO/DCE solutions were mixed with ethanol in a 13:1 rGO/DCE:ethanol ratio by weight. For rGO inks using butanol instead of ethanol, the same weight ratio was applied.

### 3.2.3 Film Deposition Procedure

Films were deposited using a using a 6cm x 25cm polytetrafluoroethylene (PTFE) Langmuir trough (Kibron Microtrough G1) with a 0.4cm x 0.4cm x 0.1mm platinum Wilhelmy plate . To prepare the surface for deposition, the barriers were closed to their fullest extent, then the entire surface was cleaned via surface aspiration before expanding the barriers to their desired width. The surface

pressure monitoring was then baselined to this clean interface, and a "test" barrier compression was run to ensure the interface was truly clean.

To begin deposition, the nanomaterial ink to used was then transferred to a glass syringe connected to a PTFE tube with an inner diameter of 0.33 mm. A syringe pump was used to deposit the ink at a rate of 0.1 mL $min^{-1}$. The end of the PTFE tube was then placed above the air-water interface so that the ink droplets would hit the surface immediately after falling from the tube but would not touch interface until the droplet had left the tube. The deposition was continued until the interface was covered enough nanomaterial film such that the dispersant from the previous droplet did not have enough time to fully dissipate before the subsequent droplet fell; either that, or the encroaching film limited the free interface enough so that instead of the droplet spreading on the surface, it formed a liquid lens. In both cases, this was usually approximately a circular area with diameter 2cm.

For films that were to be transferred to a substrate, the substrate was placed on a glass slide to raise it from the bottom of the trough and placed into the subphase water before deposition. After the deposition was completed, water was removed by placing a vacuum siphon on the side of the barrier without a nanomaterial film. The flow rate of this siphon was adjusted so that the water was removed dropwise.

### 3.2.4 Processing Surface Pressure Data

Root mean square (RMS) amplitudes were calculated using both the raw data, and a Savitzky–Golay filter of that data with width 81 and order 1. RMS amplitude was then calculated as the root of the squared difference between the raw data, and the filtered mean across a window of 50 datapoints (12.5s). This method was adapted from Silverberg et al [39].

### 3.2.5 Film Deposition Videography and Kymograph Preparation

Videos were recorded at a resolution of 1920x1080 pixels on an iPhone 12 at 30 frames per second using the e2eSoft iVCam video capture software. For consistency, the same lightings were used for each video, and the camera was held a uniform 40cm above the dripping interface. To prepare a kymograph, the captured video was split into frames using the software ffmpeg with a frame sampling rate of four images per second. This means that the final kymograph (to be defined in the next section) has a time resolution of 0.25s per pixel on the time axis. From there, the image stack was loaded into the software FIJI Is Just ImageJ (FIJI) as a virtual stack and converted into a set of

32-bit greyscale images. The area of interest was selected as a line that was in the center of the experimental trough and stretched from the barrier to the dripper at the center. The video was then converted to a kymograph through the Image -> Stacks -> Reslice option. Brightness and contrast were then adjusted for clarity.

### 3.3 Surface Pressure Perturbations as an In-Situ Monitoring Method.

The most direct measurement of a Langmuir films' in-situ viscoelasticity is a interfacial rheometer. These devices work by suspending a small wire in the interface, actuating it with minute amounts of force, and observing the resulting strain in the film [40]. While such instruments would provide useful and direct monitoring of the film properties, they are unsuitable for this application. Not counting the significant expense of an interfacial rheometer, the dispersant compressed jammed films studied here are formed in highly dynamic systems. This film mechanism would likely be disrupted by the confined geometry of an interfacial rheometer, and the spreading force of the nanomaterial ink would likely damage the highly sensitive probe.

Instead, inspired by work from Silverberg et al., it was proposed that oscillations in the surface pressure of the film could be directly tied to the mechanical properties of the film, and therefore a measure of the film's transition to rigidity [39]. In this way, they could act as a proxy rheometer. Silverberg et al. show that under traditional barrier compression, where a low-density film is deposited on the interface and then compressed with physical barriers, small force oscillations are translated to the film due to the mechanics of the stepper motors powering the compressing barriers. These force oscillations were then seen in the resulting surface pressure of the film, as the force itself was translated through the film to the Wilhelmy plate or platinum probe. Using these force perturbations, a rudimental dynamic mechanical analysis was conducted using a simple spring and dashpot model, and this was used by Silverberg et al. to determine film transitions from viscous, to viscoelastic, and finally elastic regimes (Figure 7).

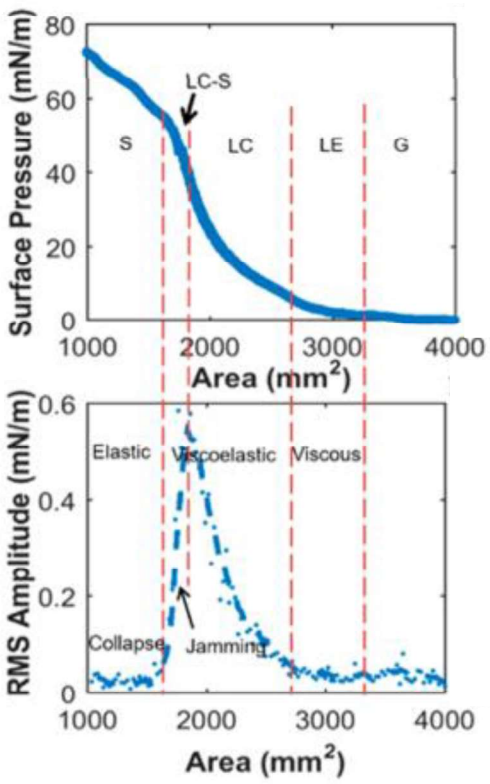



**Figure 7:** (Top) Surface pressure vs area isotherm for a monolayer of 1 μm silica spheres deposited on the air-water interface. (Bottom) Root mean square (RMS) amplitude of surface pressure oscillations due to the stepper motor's mechanical force oscillations. Reproduced from [39]

Since our film deposition system also applies a periodic force to the growing film in the form of repeated droplets of material ink, it was proposed that a similar analysis might be possible for in-situ measurement of our system.

Initial investigations showed promise, and there appeared to be a trend in film formation. Figure 8 shows the surface pressure trend for a deposition of $MoS_2$. Notably, as the deposition progresses the amplitude of the surface pressure pulses increases, which would be expected with a film becoming more elastic. This can be seen in the root-mean-square-error measurement of surface pressure.

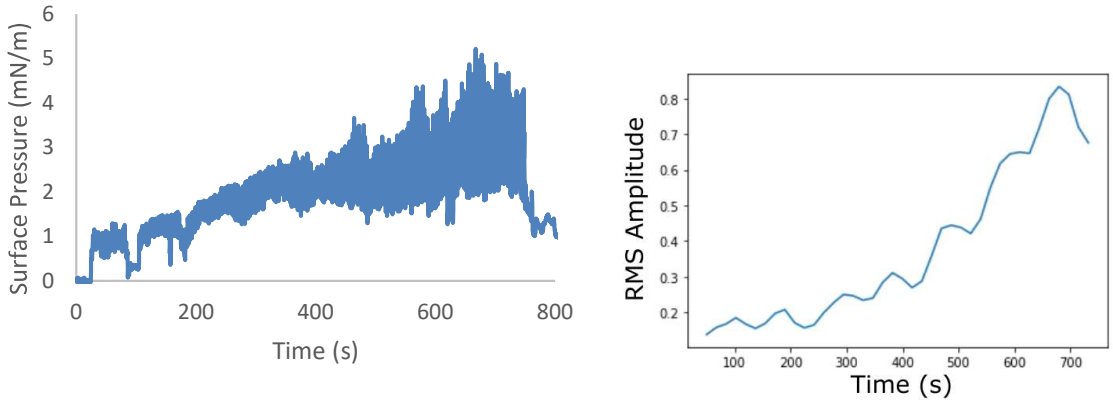



**Figure 8:** (Left) Surface pressure over time for an $MoS_2$ deposition. The width of the signal is due to repeated spikes in surface pressure from additional droplets being added to the surface. (Right) Root mean square (RMS) amplitude of the signal on the left.

However, despite the promise of the initial investigations, this method showed high deviation in repeat trials. The surface pressure signal proved to be highly sensitive to the initial position of the platinum measurement probe, and the depth of this probe in the interface. This lack of repeatability precluded using this as a measurement technique, as one could never be sure if new features were the result of slight differences in experimental setup, or actual measurements of new behavior. It is possible that with multiple probes in the interface (taking measurements from multiple areas across the film), a greater understanding of the surface dynamics, and a more sensitive measurement, this technique could be refined to the point of applicability.

## 3.4 Visual Characterization

Until now, visual observation of the film dynamics was used as the main method of investigating the film's rigidity. Due to the failure of surface pressure perturbations as a direct measurement of the film's physical properties, it was proposed that a more rigorous visual method could be used. Figure 9 shows example images of a film as it is deposited. As Figure 9 shows, distinguishing between the states is relatively simple by visual inspection. However, there remained 2 challenges. Firstly, the total time of film deposition can take as little as 5 minutes, and as long as 12 hours depending on the concentration of the nanomaterial ink. The dynamics of the film, and its transitions to a jammed film need to be studied over the entire time period. Succinctly put: an 8-hour video is not a data-point. Secondly, determining and identifying key points within the deposition needed to be done in a

repeatable way. It is not enough for an experimenter to watch the video and identify points of interest; instead, we needed a repeatable method to identify changes in the film morphology, and phases of the deposition.

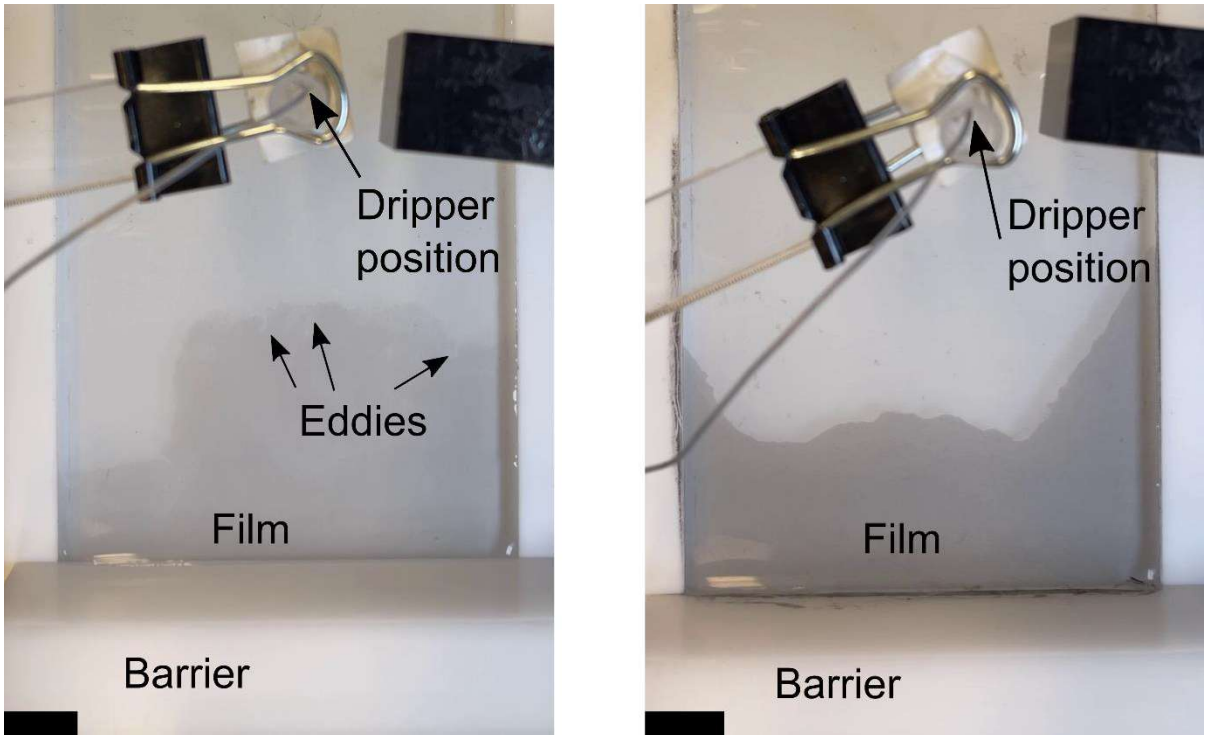



**Figure 9:** (Left) Image of a reduced graphene oxide (rGO) film in the free-flowing state, and (right) image of the same film after it has solidified into the rigid state. Note the vorticities present at the film edge in the free-flowing state. Scale bars are 1cm.

To this end, a data processing technique known as a kymograph was employed. The kymograph was first invented by Carl Ludwig in the 1840s, it is a space-time plot where a particular variable is measured over time, with one axis representing space and the other representing time [36]. This technique was expanded to videos by Jan G. Švec, as a method to examine the high-speed vibrations of human vocal cords in 1996 [41]. In this technique, a single line of pixels in a video is identified as the area of interest. Then, the pixels in that line are sampled from each frame of a video and arranged side by side. In this way, one forms a still representation of the dynamics of that region over time. A visual representation of this is shown in Figure 10.

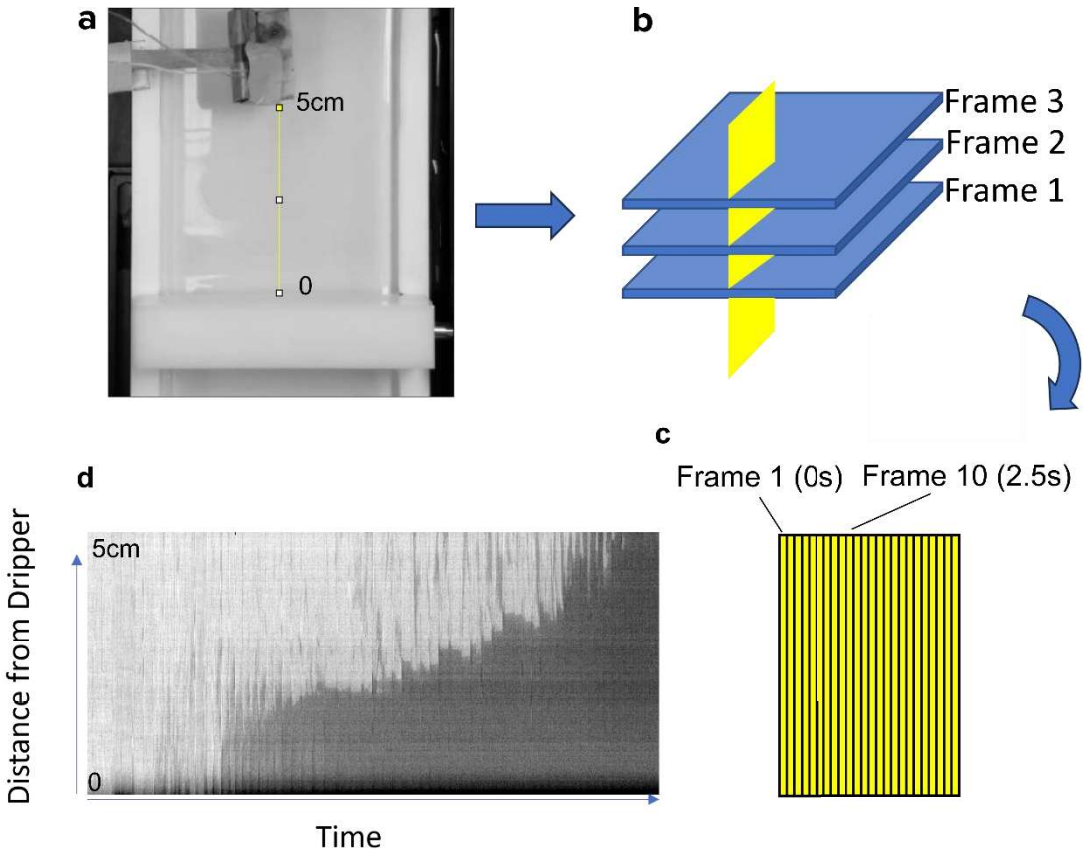



**Figure 10:** Diagram showing the processing making a kymograph. The vertical yellow line in the (a) corresponds to the vertical array of pixels that is sampled from each image. (b) Shows a depiction of the process acting on every frame of the video, resulting in (c), a diagram showing each pixel array being arranged sequentially. (d) The final kymograph image.

The resulting kymographs show the story of a particular film's growth. By sampling only from a line of pixels and at a particular interval: the kymographs frame rate, transient effects like ripples in the interface, small particles floating on the surface, and other effects are filtered out. Instead, the growth of the film over time made clear. In the image shown in Figure 10 (d), the dark grey corresponds to the film, where the light section corresponds to free interface. The vertical stripes

correspond to new droplets of nanomaterial ink hitting the interface, creating surface waves, and pushing material back on the surface.

## 3.5 Conclusion

In this chapter, two film characterization methods were proposed and evaluated. While in-situ characterization seemed a promising method to analyze the mechanical properties of growing 2DLB films, in practice the technique proved unreliable in our setup. Perhaps with more study the shortcomings of high sensitivity to initial placement of probes and an overall lack of repeatability could be overcome. Instead, a video characterization method was proposed to monitor the film's rigidity. While this is an indirect method of film analysis, it has the advantages of being insensitive to the film deposition conditions, does not affect the deposition of the film, and leverages existing observations about the visual characteristics of a jammed and flowing film. A kymograph was then shown to be a successful technique to process the long duration videos into digestible figures that made significant points in the deposition clear. This technique will be heavily used in the following chapters to analyze the growing films.

# Chapter 4
# Jamming and Phase Transitions in Spreading Compressed Langmuir Blodget films of 2D Materials

## 4.1 Introduction

In the following chapter, containing much of the significant work of this thesis, attempts to identify and explain why sometimes a nanomaterial film is deposited as a rigid film that starts at the edge of the trough and grows inward, and sometimes remains as a flowing film that is uniformly distributed over the entire interface. From there, how the film initially forms is investigated, along with the morphology of the initial growing film and the final film. This is done for both jammed and unjammed films. In addition, parameters are determined that cause a film to be deposited in the jammed, or unjammed state, and some of the options to induce a film deposition in either regime. Finally, a mechanism of how the film jams is proposed.

## 4.2 Experimental

Films in this section were deposited using the methods mentioned in 3.2, except where indicated otherwise.

### 4.2.1 Determination of Solid Phase Material Ejection Speed

To determine the ejection speed of the ablated material at the edge of the solid phase film, videos were captured using the procedure mentioned in 3.2.5. From there, each frame (30 frames per second) was extracted as a still image and loaded into FIJI. Distinct particles were manually tracked as they broke away from the film front, and their speeds were calculated from the average speed over the first 0.5s of their ejection.

### 4.2.2 Brewster Angle Microscopy

A fixed angle Brewster angle microscope (BAM) (KSV Nima) was used with a 14 cm distance between the two barriers. The dripped was placed in the center of the trough, midpoint between the barriers. The position of the BAM field of view was placed as close to the barriers as possible without the height of the barrier disturbing the BAM's incident laser. In practice, this was approximately 3cm

from the barrier. The prepared $MoS_2$ mixture was then dripped onto the surface. For the jammed film, the stock as-prepared concentration was used, whereas for the not jammed film, a 1 in 8 dilution (with the same 1:3 DCE:DMF ratio) was used. Since the droplet, spreading, and evaporation disturbs the interface, dripping had to be paused each time a BAM image was taken in order to obtain a resolved image.

### 4.2.3 Langmuir Areal Concentration

Langmuir areal concentration was measured by first performing a 2D material film deposition until the interface was covered enough nanomaterial film such that the dispersant from the previous droplet did not have enough time to fully dissipate before the subsequent droplet fell. From there, the film was compressed to a surface pressure of 30 mN/m, at a barrier compression speed of 50 mm/s (30 $cm^2/s$). 30 mN/m was chosen as it was very close to the threshold of monolayer collapse for many Langmuir films of 2D materials [23], [39]. From there, the final trough surface area at this pressure was divided by the total solution deposited to obtain the Langmuir areal concentration.

### 4.2.4 Spreading force dissipation distance

The spreading force dissipation distance was determined by depositing a small amount of material in the jamming growth mode, until there were small clusters of gaseous phase material on the interface. From there, videos were taken as further solution was dripped onto the surface. The particles on the surface were then pushed by the spreading front and served as a marker of this front while providing minimal disruption to it. Particles speeds were then determined by frame-by-frame analysis in FIJI, and the spreading film front was taken to be dissipated once the particles slowed to an un-measurable speed.

### 4.2.5 Particle Tracing using TrackPy

Videos were taken of growing films and separated into still images using the method previously described in 3.2.5. From there, brightness and contract were adjusted for clarity through FIJI, and image sequences were analyzed using TrackPy 0.5.0 with the following parameters: particle size = 15, particle mass = 200, and a threshold = 5.

## 4.3 Jammed and Flowing Films

Figure 11 shows a both a flowing and jammed nanomaterial ($MoS_2$) films being deposited dropwise on the subphase water surface. As mentioned in the introduction, normally when nanomaterial dispersions are dripped onto the surface, the resultant Langmuir film is formed of particles free floating around the surface. However, if a particular material-ink and trough setup are used, the deposited material is pushed to the to the edge of the trough with each droplet and causes a film to build up from the edges. From the edges, the film grows inward towards the dripper. This we call a jammed film. However, outside of these particular conditions the material never condenses into a film and remains uniformly dispersed on the interface, and as deposition proceeds the entire film largely densifies uniformly. This we call a flowing, or not jammed film. The goal of this work is to probe when and why jamming happens, and how to induce it.

To study the conditions under which a nanomaterial film will jam, it is imperative to differentiate between a jamming film and a flowing one. This can be somewhat difficult because the timescale of the deposition (minutes) and transparent nature of the material film may deceive the observer. Here, the kymographs mentioned in section 3.4 provide clarity. Figure 11c, d shows two example kymographs from jammed and flowing films. For a flowing film, the material is spread uniformly on the interface. When the next droplet of nanomaterial ink hits the surface, it pushes back the film, forming an area of free interface in the center of the trough. When the dispersant from the droplet has evaporated, the compressed material relaxes and bounces back to cover the whole trough once again (Figure 11). This is reflected in Figure 11c; the flowing film is uniformly distributed about the interface – resulting in a uniformly grey image that becomes darker over time as the film becomes denser. The vertical stripes are the moments of free interface caused by the nanomaterial ink droplets hitting the water and pushing the film back.

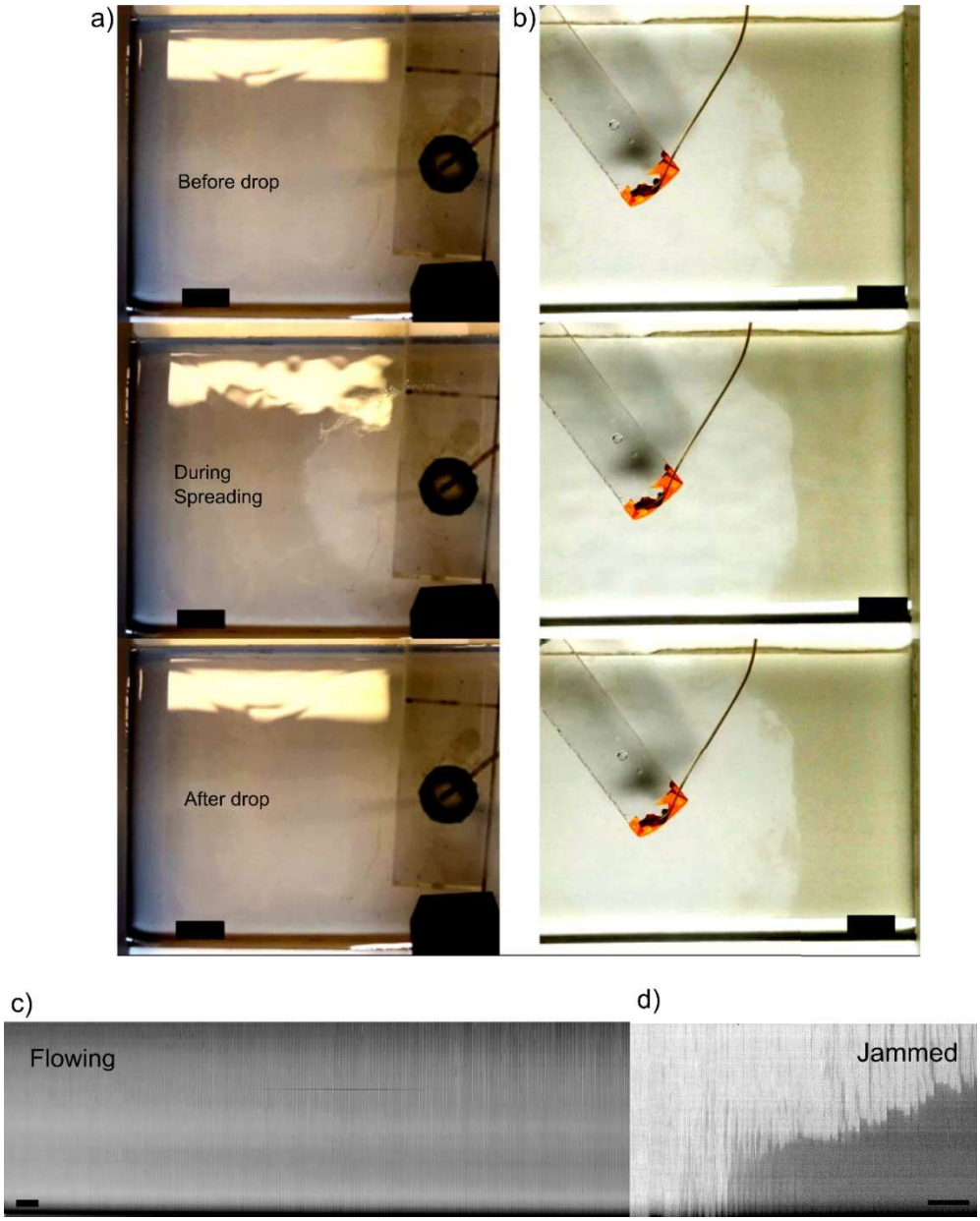



**Figure 11:** Still images from the deposition of $MoS_2$ Langmuir films have either a) not jammed and remained flowing throughout the deposition, or b), jammed and became rigid during deposition. A) and b) show still images of the film deposition before, during, and after a material ink droplet spreads on the surface. Scale bar is 1cm. C and d) show the resulting kymographs for the flowing and jammed films respectively. Scale bar is 20s. As the MoS2 film is somewhat transparent, the top and bottom image sets' brightness and contrast have been heavily edited for clarity.

In the jammed case, the film is rigid enough to resist the force applied by the spreading ink, and little change is seen in the film edge. Similarly, the kymograph in Figure 11d shows a distinct film edge which grows over time.

One insight that can be gained from a kymograph is the relative density of the film during deposition. This is especially helpful as measuring the film density usually requires depositing the film or taking a compression isotherm, both of which end the deposition. The relative density is indicated by how dark the film is, a denser film will have more material in the area that pixel covers, appearing darker visually. This is measured by the pixel grey value of a line of pixels from a kymograph, darker pixel corresponds to a lower grey value. Figure 12 compares the grey values of $MoS_2$ depositions both a jammed and flowing film as the film deposition proceeds. It shows that the density of jammed film is much higher than that of a comparable flowing film with the same amount of material deposited. For flowing growth mode films, the density decreases gradually and linearly as the deposition proceeds, plateauing when the interface is full. Conversely with jammed films, the density falls sharply at the beginning of the deposition and remains mostly constant. The figure also shows how jammed films reach a higher final density than films grown under not jammed, or flowing, conditions, even at the end of material deposition.

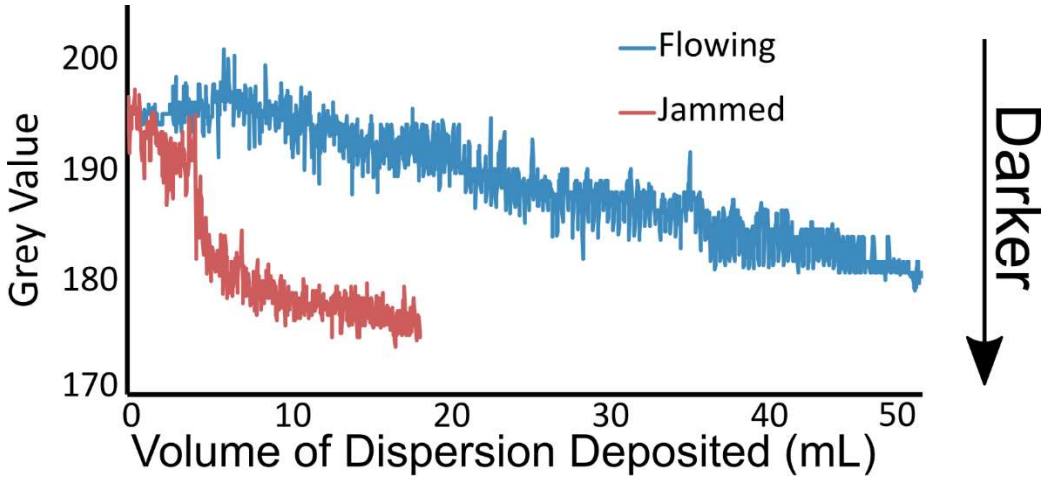



**Figure 12:** Pixel grey values for both jammed and flowing films of $MoS_2$. A darker pixel corresponds to a lower grey value.

## 4.4 The Phases of Jammed Film Growth

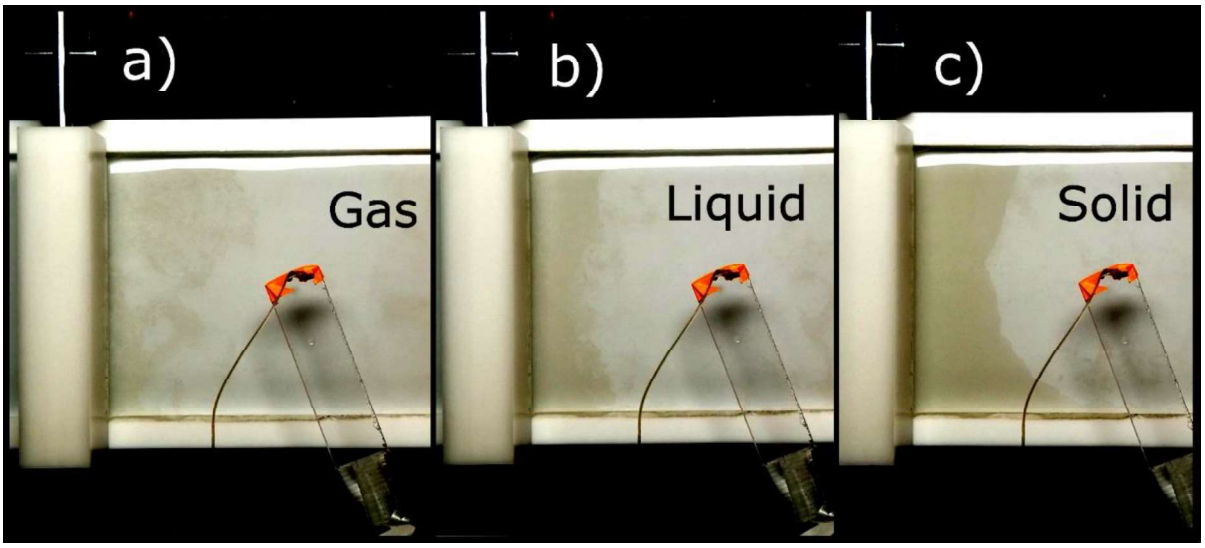



**Figure 13:** Stages of film deposition for a jammed film of $MoS_2$ showing the a) gaseous, b) liquid and c) solid phases. Brightness and contrast have been heavily edited for clarity.

Figure 13 shows the progression of jammed film being deposited, and the three phases of jammed film growth that have identified. Specifically, it shows a dilute dispersion of MoS2 that has been dripped on the surface of the water trough. Shortly after the deposition has started, the film begins as small floating clusters that move freely on the surface (Figure 13a). Here, there is no clear dividing line between the film covering the subphase water, and the free interface. We call this the gaseous state of jammed film growth as it is analogous to the gaseous films of lipid layers, where the molecules typically float freely on the interfacial area. Continued deposition causes these particles to condense into a continuous domain located at the edge of the trough (Figure 13b). The film now has a defined edge, a clear dividing line between film and free interface, and does not float freely over the trough area but remains fixed at the edge between droplets. The film still deforms under perturbation from the next droplet, but it does not re-disperse into discrete particles or clusters under this applied pressure from subsequent spreading droplets. Notably, the film is now also stable under small perturbations like air currents or vibrations that would disperse the gas film – meaning the film is meta-stable if the procedure is suspended at this point.

Continued deposition moves the film into the solid phase (Figure 13c). Here, a clear film edge is formed, and this edge does not deform under the spreading pressure of additional droplets added to

the surface. Indeed, at this point the film, not only sustains stress without deforming, but appears to store that stress elastically, ejecting clusters of newly deposited material from the edge after each droplet at speeds up to 20 mm/s. The film is rigid but is not compressed into a fully dense film as traditional barrier surface compression can reduce the film area up to 40% (Figure 14).

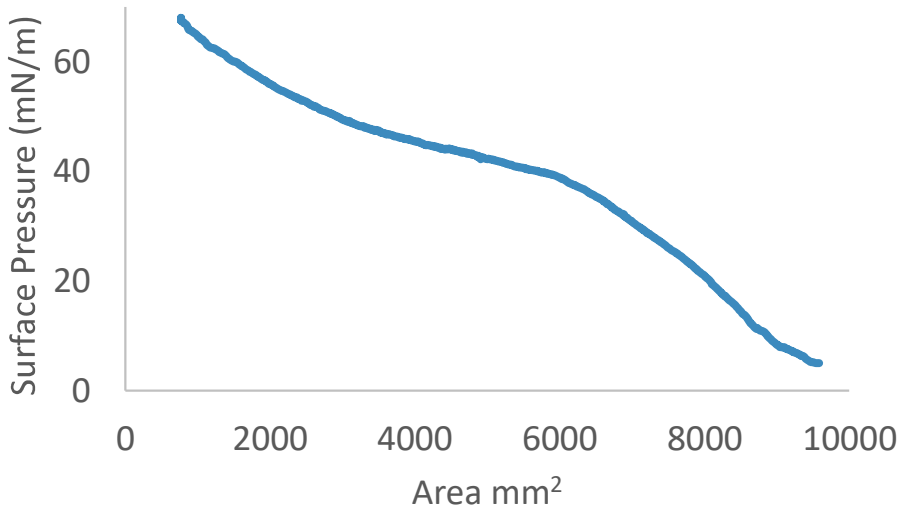



**Figure 14:** Compression isotherm of a jammed rGO film. The "kink" at approximately (6000, 39) indicates monolayer collapse and the maximum film compression [25].

At the start of the deposition, particles in the gaseous film state are flowing freely on the surface, and only briefly pass through the sampled area, leading to the light region seen in the figure. As the film solidifies, particles will spend more time in the sampled region, leading to a darker colour. As shown in the figure, the transition from a gaseous phase to a liquid phase is abrupt, and immediately forms a film with significant width from the edge. Only a few drops of material can induce this change. This abrupt phase change is one of the key features in jammed interfacial films. The transition from liquid phase to solid can also be seen in the film front. In the liquid phase, the film front is subject to deformation, and in the image presents as a diffuse region in front of the film. When the film front stops deforming, this indicates a transition to the solid phase. This transition too is abrupt, although somewhat less so than the gas-liquid phase.

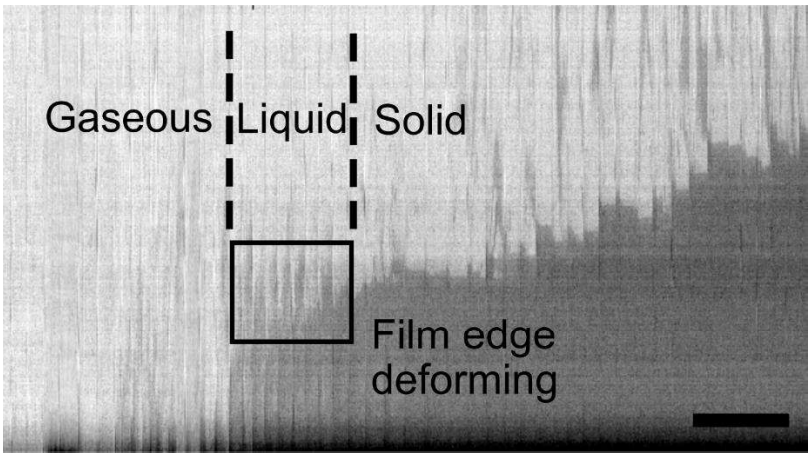



**Figure 15:** Kymograph of a jamming MoS2 film deposition. Gaseous, liquid, and solid phases, as well as the deforming film edge are indicated. Scale bar is 20s.

In contrast to the flowing case shown in Figure 13c, the kymograph of the deposition of a jammed film shows distinct features (Figure 15). At the start of film deposition, particles in the gaseous film state are flowing freely on the surface, and only briefly pass through the sampled area, leading to the light, uniform region seen in the figure. After enough material has been deposited to the surface, the film abruptly transitions to the liquid phase – a key feature of the jammed films. This is indicated by the sudden darkening of the film over the gaseous to liquid transition line. Notably, despite the rate of material addition being held constant, the change to the liquid phase happens over a very short time - often requiring only one or two droplets of material dispersion. This is indicative of a first order phase transition, but a rigorous analysis into the order of this transition was not carried out. In the liquid phase, the film front is still subject to deformation, and in the image presents as a frayed edge over the solid, dark, region indicating the rest of the film. The sold phase is identified by the film front strengthening and resisting deformation, which is reflected in the kymograph as the edge of the dark film region becoming distinct and defined. This transition too is abrupt, although somewhat less so than the gas-liquid phase transition.

## 4.5 Investigating the Conditions that Cause Jamming

To investigate the conditions under which a film will jam, films of different materials, dispersants, and concentrations were deposited with the goal of creating a Langmuir nanomaterial jamming phase

diagram. In Figure 16a, we measured the conditions that cause jamming for dispersion of rGO in ethanol/1,2-dichloroethane (DCE), rGO in butanol/1,2-dichloroethane, and $MoS_2$ in dimethylformamide (DMF)/1,2-dichloroethane at various concentrations.

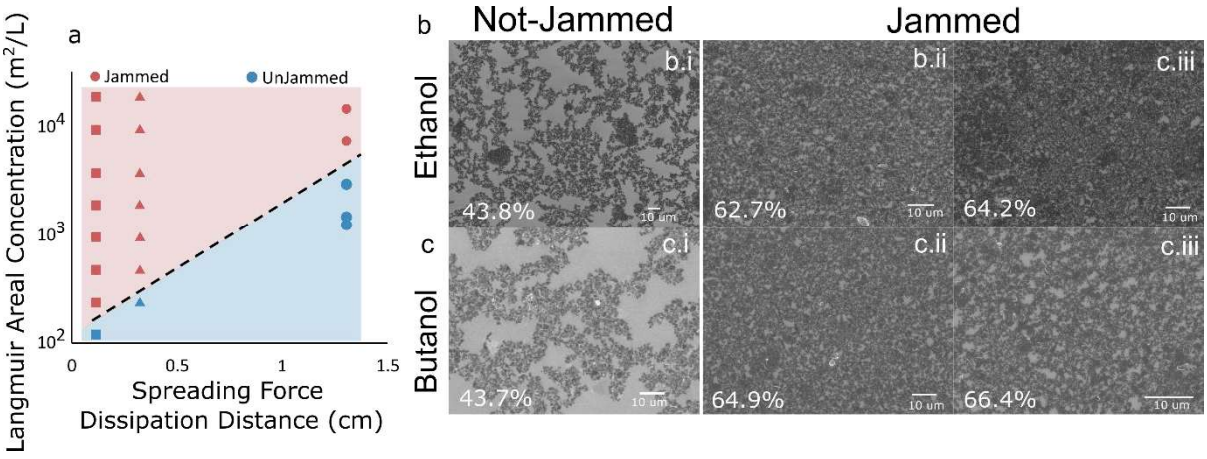



**Figure 16:** a) A phase diagram indicating the conditions under which the nanomaterial film will jam under deposition. The y axis corresponds to the Langmuir areal concentration, the areal concentration of the solution as measured by a Langmuir trough. The x axis corresponds to the distance from the barrier where the spreading force from the ink droplet dissipates. Square, triangle, and circle markers correspond to rGO in butanol/DCE, rGO in ethanol/DCE, and $MoS_2$ in DMF/DCE respectively. b) Scanning electron microscope images of rGO films deposited at various concentrations and spreading dispersants. White numbers indicate the packing fraction of the film obtained by image thresholding from N=5 different images of the film at different magnifications and areas. Scale bar is 10 μm in all images. Films in b).i-iii used ethanol as the spreading dispersant with an area concentration of 472 $mm^2$/ml, 944 $mm^2$/ml, and 9442 $mm^2$/ml respectively. Films in c).i-iii used butanol as the spreading dispersant at an areal concentration of 236 $mm^2$/ml, 472 $mm^2$/ml, and 9442 $mm^2$/ml respectively**.**

Preliminary work had identified that whether a particular deposition would form a jammed film most significantly depended on the nanomaterial concentration, and "spreading ability" of the dispersion ink. The dynamics of how a dispersant droplet spreads on water are complicated, and in this case are not well described by a single spreading coefficient because these dispersion inks are binary mixtures of components with large differences in surface energy, volatility, and viscosity; and in turn are being added to a dynamic system where the interface is constantly changing both chemically and mechanically. To quantify the contribution of the spreading dynamics on the system

made when determining whether a deposited film will jam, we drew insight from jamming theory and hypothesized that the parameter that matters most is the ability of the spreading droplet to force the interface material into a small region at the edge of the trough. Packing fraction is one of the critical parameters of jamming theory, and usually determines whether a material is jammed, therefore the ability of the dispersant to force all the material on the interface into a small region where it could jam is likely critical in forming a jammed film. In our system, this was quantified by measuring how close to the edge of the trough a droplet of dispersion could push the individual clusters of material on the interface just after the deposition began. This we called the spreading force dissipation distance. This, in turn was measured via videos of gaseous phase films just at the start of the deposition, to limit the effect existing material in the trough might have on the measurement.

Concentration was measured using a parameter we call the Langmuir areal concentration. Since the different materials studied here have different particle sizes, densities, atomic composition, and average layer numbers, a typical mass or molar concentration does not truly reflect the effective concentration in this system. Instead, the concentration most critical here was the amount of interface area covered by the material in a known volume of solution. This areal concentration more accurately reflects how much the interface is being changed with the addition of new material. This areal concentration was determined by taking the amount of solution needed to create a high-density Langmuir film of a certain area, hence Langmuir areal concentration.

The results in Figure 16a show a critical spreading-concentration relationship that determines whether a film will jam. It shows that there is a critical transition point where either the material concentration or spreading pressure are high enough that a critical local packing fraction is reached during film deposition. If this critical packing fraction is reached, the material locally jams, and a jammed film is grown; however, if this packing fraction is never reached (either due to not enough local material, or it not being compressed enough by the spreading dispersant), the material will never jam, no matter how long the deposition continues or how much material is added to the surface. It is notable that Figure 16a contains multiple materials of varying particle sizes, indicating that the identified spreading-concentration relationship is a core property of the system and not merely true for one material system.

To confirm that there was an actual transition between the jammed and unjammed regions of Figure 16a, films of rGO were made using conditions on either side of the jammed-flowing line, as

well as sampled from significantly into the jammed region. These films were then deposited on silicon substrates for SEM analysis using the horizontal deposition method. The packing fractions of these films were then calculated using image thresholding. The results are shown in Figure 16b, c. There is a sharp difference in film morphology between films deposited in both the flowing, and jammed state. The flowing films is made of a networks of loosely packed string like structures spanning the film and is accompanied by a lower packing fraction. For jammed films, the structure changes to a closely packed arrangement of rGO sheets with voids between them. The packing fraction of the jammed film is significantly higher than that of the flowing film; increasing the concentration of the dripping solution into the jamming region causes the morphology to change to closely packed particles and is accompanied in a sharp increase in the packing fraction by ~1.4 times to 62.7% (Figure 16b.ii).

When the concentration of nanomaterial in suspension is significantly increased past the jamming point, moving the deposition conditions much farther into the jammed region, there is little change in packing fraction and morphology. This is in strong agreement with jamming theory and is evidence that the film itself is truly in a jammed and unjammed state. Interestingly, the packing fractions of the jammed films are within the range predicted by computational studies of polydisperse attractive particles, although somewhat lower than the most common prediction of ~70%, depending on the studied conditions [32], [42], [43].

## 4.6 Probing the Mechanism of the Jamming Transition

To probe the nature of this phase change, an ink suspension of rGO in a DCE/ethanol suspension was deposited in the trough until the film was about to transition from the gas to liquid state. The ink was then replaced with a pure DCE/ethanol mixture of the same composition as the rGO suspension, only without the nanomaterial. This was to separate the two effects on film formation: the addition of material and the applied spreading pressure from the droplet. It was assumed that the pure dispersant ink should have similar spreading dynamics to the nanomaterial containing ink. Despite having similar spreading dynamics, the pure dispersant ink was not able to transition the film into the liquid phase, even though the film had repeated compression due to the spreading pressure of the pure dispersant ink (Figure 17). For comparison, Figure 17b shows a typical jamming deposition under the same conditions as Figure 17a, and displays a rapid transition to the liquid and solid phases.

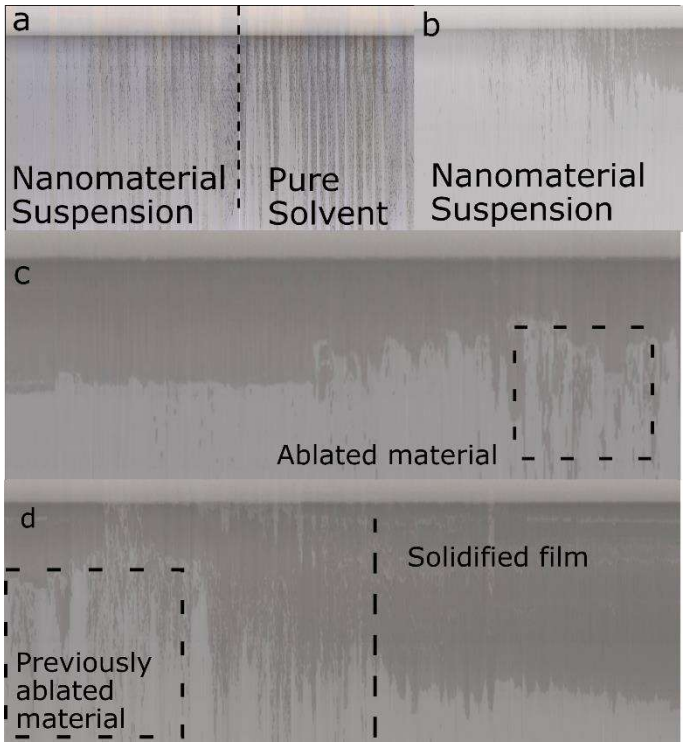



**Figure 17:** A kymograph of rGO deposition where the ink was switched to a pure dispersant mixture before the liquid state was reached, which we hypothesized would condense the film without the addition of material. Instead, the material remained in the gas phase. b) Kymograph of a typical rGO deposition for comparison with a), showing the transition to a liquid and subsequently solid phase film at the right side of the image. c) Kymograph of a liquid phase rGO film being subjected to the dripping of an ink composition with only dispersant, no nanomaterial, showing the ablated material from the film edge. d) Kymograph of ablated liquid film from c) resolidifying after a return to a rGO suspension as the deposition ink.

This experiment was then repeated, except this time the deposition was continued until the film reached the liquid phase. When the pure dispersant was dripped into the trough containing an rGO film in the liquid state, rather than solidifying the film, the pure dispersant broke up the liquid film by ablating the film edge, reverting the film into a similar form as the gaseous state. (Figure 17c). Then, rGO nanomaterial was re-introduced into the ink, and the film re-condensed into the liquid state and proceeded to solidify as normal (Figure 17). Both of these experiments indicate that the applied compression from the spreading droplet is not enough to induce a material to change phase, and

instead both the presence of the spreading force and added material are necessary to induce a phase change.

This observation, combined with insights from jamming theory, provides an indication of the mechanism of phase change. Originally, with a low amount of material on the interface, the nanomaterial sheets, or small aggregated domains of the sheets, float freely in response to deformation. In this state, the fluid flow on the interface is primarily driven by the spreading of the material ink on the surface, and the flow of the ink's spreading front expands out radially from the deposition point. Then, when confined by the width of the trough, changes to a uniform spreading front that finally hits the Teflon barriers at the end of the trough (Figure 18a). This collision induces vortices in the flow near the barriers (Figure 18c). With each drop, the material in the trough is pushed into the vortexed region by the spreading droplet. As successive droplets deposit material, the local packing density starts to increase in these vortices until there begins to be cluster-cluster interactions. Once again taking insights from jamming theory, Ji et al show how the increase in local packing density causes an increase in viscosity, and a similar interfacial viscosity change is expected here [44]. This increased viscosity reduces the turbulence of the spreading front in these high-density locations, and the combination of the increased density and uniform compressive stress causes the material to compact further and transition to a liquid film. Once the transition to a liquid film has been made, it exists at a lower energy packing state due to small attractive forces between particles. These forces are assumed here. The liquid film is then continually densified until it begins to behave as a jammed visco-elastic solid – the solid phase.

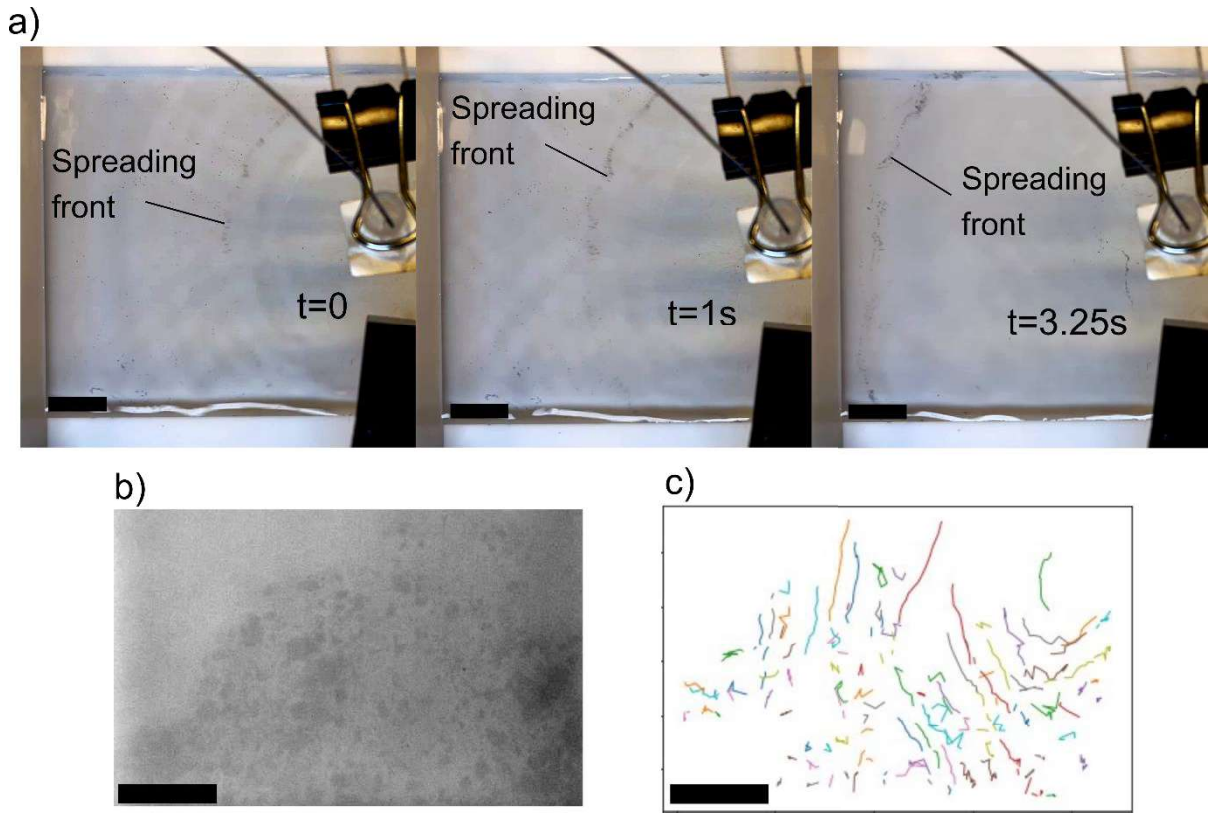



**Figure 18: a)** Image sequence of an rGO deposition showing the dispersant spreading front. b) Image of an $MoS_2$ film deposition showing particles on the surface. Scale bar is 1cm c) Particle traces of the movement of the particles in b) after the spreading front had dissipated, generated using TrackPy over a period of 3s. Scale bar is 1cm.

Figure 19a shows Brewster angle microscopy images of the microstructure of a growing film for a film deposited in unjammed regime alongside that of a jamming regime (Figure 19b). While the gaseous phase of the jamming regime can look visually similar to an unjammed film, imaging of the microstructure reveals there are differences present from the beginning of the deposition. Figure 19a shows the initial stages of an unjammed, flowing film of $MoS_2$, where "string-like" clusters of material float on the surface. This can be compared to Figure 19b, which shows the initial microstructure of a jamming regime film similarly early in the deposition. In the jamming regime, the gaseous film consists of islands floating on the surface rather than strings, and these islands appear to be of much higher density than the flowing case. These clusters have been reported previously, and their morphology is concentration dependent [45]. As the deposition progresses, the flowing film

deposition structure remains string like, and appears to densify via the strings becoming more numerous, whereas the jamming films appear to densify by increasing the number and size of the island like clusters. Notably, the string like clusters shown in Figure 19a show a striking similarity to the final film morphology shown in Figure 16b, despite the films being made from different materials. This suggests that the morphology of the film has much more to do with the conditions of deposition rather than the particle size or particle-particle interactions of the nanomaterial being deposited.

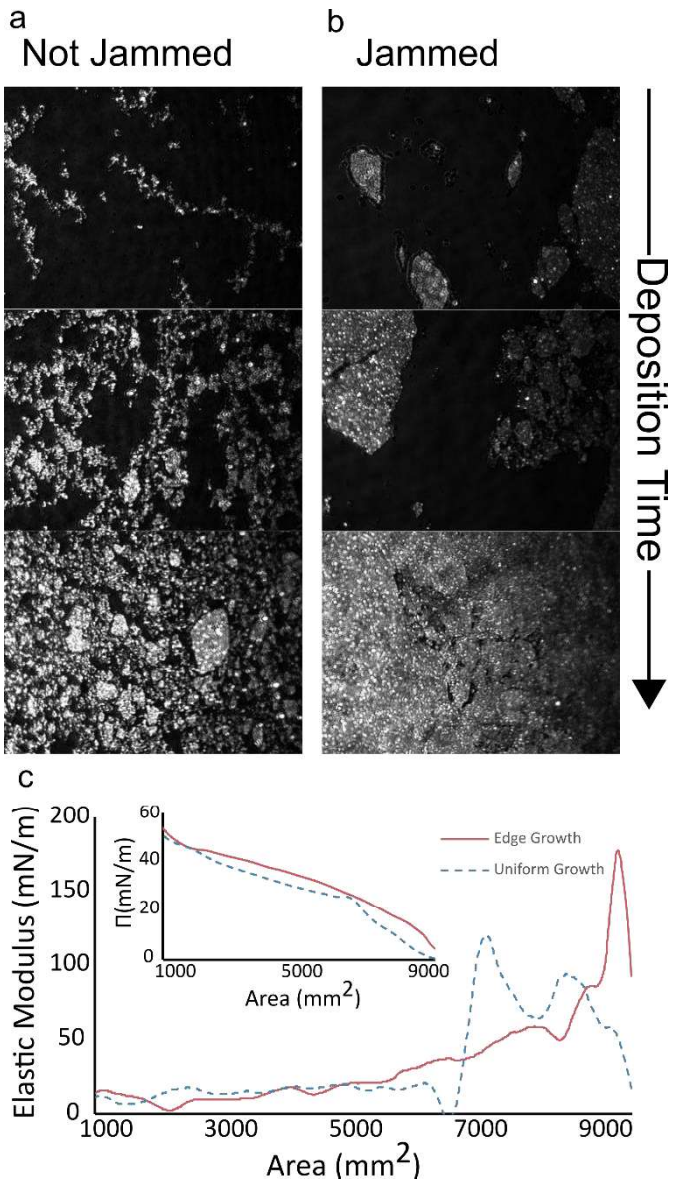



**Figure 19:** Brewster angle microscopy images showing the microstructure of growing films of $MoS_2$ in both a) the flowing growth mode, and b) the jamming growth mode. c) Elastic modulus under compression for both a jamming and unjammed film of $MoS_2$, inset shows the original compression isotherm using Π to denote the surface pressure.

The string like behavior of the flowing growth mode film shows similarities to structures predicted by Lois et al. both in terms of morphology and how they are formed [42]. Lois et all predict that an

attractive particle system can show percolative clusters well below the density threshold given by random close packing under compressive stress conditions, but those clusters are only rigid "one-way" meaning that they only resist deformation in the direction of compression. When the pressure is removed, and the deformation reversed, the clusters deform and stretch into the string like formations. In the flowing, or not jammed, the material is compressed by the spreading force of the suspension droplet, forcing it into a higher density film. When the spreading dispersant evaporates, this force is removed, and the material stretches back into the string like clusters seen in Figure 19a. This also supports the mechanism of jamming mentioned above. Without a high enough local density, the small dense islands seen in Figure 19b never form. Instead, the flowing film exists in a looser packed string like network seen in Figure 19a. This also explains how the unjammed films can undergo such significant deformation with each droplet, shown in Figure 11. The network of string like structures can support significant void space between them, while remaining interconnected, allowing for the film to cover the whole surface, be significantly deformed by the droplet spreading on the surface, and relax back to cover the whole surface once again.

In jamming growth mode films, it appears that a combination of the higher local concentration and higher spreading pressure causes the film to surpass the boundary between the one-way rigid percolating clusters and into a rigid attractive jammed system predicted by Zheng et al. among others [43]. These clusters are still small due to the gaseous nature of the film but remain rigid when the compressive stress of the spreading droplet is removed. This is further reinforced by Zheng et al.'s findings that there exist multiple phases of jammed materials that can be accessed by increasing the packing fraction or increasing the shear. In our system, it appears the difference between forming a jammed film and not jammed or flowing one is whether the local concentration and spreading force is high enough to force the system across the transition between a flowing system and an attractive jammed system.

Further evidence for this can been seen when a jammed and unjammed film are compressed, with the same amount of material deposited. Figure 19c shows the elastic modulus $E$ calculated from a compression isotherm of both a jammed and unjammed film. The elastic modulus was calculated from $E = -A\frac{d\Pi}{dA}$, where $A$ is the trough area and $\Pi$ is the surface pressure. With the jammed film, immediately upon compression there is a sharp increase in the elastic modulus, and corresponding surface pressure, followed by a sharp decrease after peaking. This is indicative of a film that is fully

rigid, and the sharp peak is a key feature of $MoS_2$ sheets buckling and forming a second layer to relieve the stress in the film [25]. This is consistent with a fully jammed film, as each particle is surrounded by enough nearest neighbors to prevent any in-plane relaxation. Notably, this happens in the jamming growth mode film at a surface pressure lower than 30 mN/m, the surface pressure where collapse was previously observed by Bodik et al.[25]. This suggests the presence of stable voids in the jammed film, that lower the overall surface pressure but due to the film's rigidity are not removed under compression.

Compared to the jamming film, the unjammed film shows remarkably different characteristics under compression. The elastic modulus begins small, and then grows before finally showing signs of monolayer collapse at ~7000 $mm^2$. The small initial elastic modulus, and the ability of the film to compress a significant amount before monolayer collapse shows how the flowing growth mode film retains the ability to relax, and that the individual particles are not jammed. Instead, they are able to re-arrange and re-organize under applied stress.

## 4.7 Conclusion

In this chapter, the difference between a jammed and flowing, or unjammed, film was defined in our system, and their respective behavior during film deposition was shown. It was then demonstrated how each of these respective film deposition regimes presents on a kymograph of the deposition. From analysis of these kymographs, it was shown how a jammed film quickly reaches a high density, whereas an unjammed film takes much longer to densify, and may never reach the final density of the jammed film.

Within the jamming regime, 3 phases of film growth were identified, the gaseous, liquid, and solid phase, and an analysis of how each phase acts during deposition was presented. It was then shown that the transitions between each of these three phases are sudden. Furthermore, it was shown that these phase transitions require not only continued deposition with the highly spreading dispersant ink, but also the continued addition of additional material.

An investigation was then conducted into the conditions that determine whether a film will be deposited in the jammed or unjammed regime. Two parameters were identified, the concentration of the material ink, and the spreading ability of the ink's dispersant. A phase diagram was constructed where it was shown that film depositions could be divided into jammed and unjammed regions based on their spreading ability and concentrations. The morphology of both jammed and unjammed films

were then examined under SEM, and a significant increase in packing fraction was seen for the jammed films, which held constant despite significantly increased concentration. Notably, in the analysis to make Figure 16, other parameters were originally tested in the two axes: particle size, and total spreading energy of the spreading dispersant. We had originally hypothesized that these parameters played a role in the jamming of a nanomaterial films, but in the end, they did not play a role in determining if a deposition proceeds in the jammed mode.

The initial formation of both jammed and unjammed films was then studied using Brewster angle microscopy. From the early stages, jammed and unjammed films show significant differences in their morphology, and these differences persist as the deposition continues and the film densifies. These structures where then compared to jamming theory. Using insights from the study of attractive jamming, and the results presented over this chapter, a mechanism for the initial formation of a jammed film, and an explanation for why there are different deposition regimes at all was proposed.

# Chapter 5
# Printing Edge-to-Edge, Lateral Heterostructures on Water

## 5.1 Introduction

In the following chapter, the knowledge and understanding of how to make a solid jammed film, and induce it as rapidly as possible, is used to construct films containing two materials deposited next to each other in district regions of the coating bath. These films show very little mixing between the two material domains, and are the first examples of a lateral heterostructure printed entirely on the surface of water. It is my hope that this work serves as a proof-of-concept for future work creating complex chemical and electronic designs entirely using Langmuir Blodgett films.

## 5.2 Experimental

Films in this section were deposited using the methods mentioned in 3.2, except where indicated otherwise.

## 5.3 Printing Lateral Heterostructures

This newly gained understanding of how to quickly form highly rigid films on the on the air-water interface can now be applied to construct composite films of two distinct 2D materials without the need for barriers or mechanical compression of that interface. This provides a method to engineer lateral heterostructures of edge-to-edge contacting 2D material flakes with a clean interface and little mixing between the two materials. (Figure 20a). To form this heterostructure film, rGO was deposited until the film jammed into the solid phase. This filled roughly half the trough. The film was given one minute for the water surface to settle (Figure 20b.i), and then, the remaining material that was loosely floating on the surface was removed via surface aspiration. Then, the material being deposited was switched to $MoS_2$, and the deposition proceeded as previously described. When the material is initially switched, the contact line between the rGO and the free interface is continuous, and there is little apparent rGO present floating on the free interface (Figure 20b.ii). When the initial drops of $MoS_2$ are added, the rGO contact line is ablated, and small islands break off the rGO interface and become embedded into the MoS2 film (Figure 20b. iii and iv). Figure 20c shows the effect of beginning with $MoS_2$ as the initial material, and then switching to rGO. Notably, when $MoS_2$ is the initial material, there is significantly more mixing, and numerous islands, possibly due to the

difference in spreading ability between the rGO and MoS2 dispersions (Figure 16), or the large particle size difference between the two materials.

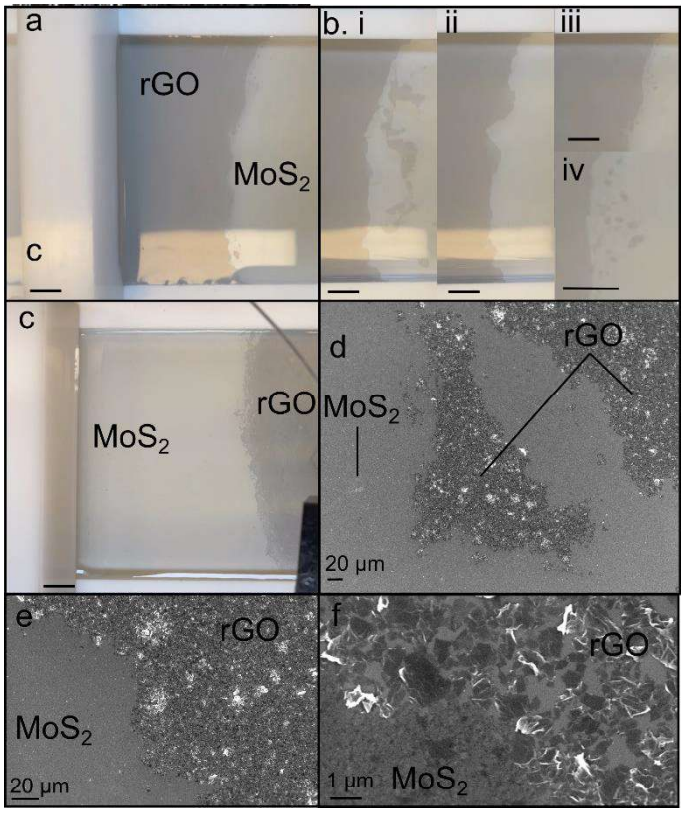



**Figure 20:** Heterostructure interfacial films of 2D materials. a) A heterostructure film of rGO and $MoS_2$, showing the two films and the contact line between them. Scale bar is 1cm. b) The film in a) just after rGO deposition i), after the interface is cleaned with surface aspiration ii), the ablated interface caused by the deposition of $MoS_2$ iii), and a zoomed in photo of that interface iv). The scale bar in b. i), ii), and iii) is 1 cm. The scale bar in b. iv) is 5 mm. c) A heterostructure film of rGO and $MoS_2$, where the $MoS_2$ was deposited first. d-f) SEM images of the film in a), showing the interface between rGO and $MoS_2$, after the film was deposited on a section of Si wafer.

Figure 20d-f shows SEM images of a heterostructure film where rGO was deposited initially. Rather remarkably, outside of the islands ablated from the initial MoS2 droplets, there appears to be almost no mixing between the rGO and MoS2 regions, and no diffusion of one material into the other (Figure 20f). This level of separation is impossible in typical interfacial films of 2D materials, where the lack of a solid, rigid film means that a second material will continuously mix when added. However, due

to the gained understanding of the jamming of 2DLB films, and how to rapidly induce it, it has instead become possible to for two distinct regions of different materials on the surface of water. Furthermore, to obtain the SEM images seen in Figure 20, the film had to be deposited onto a silicon wafer via the horizontal deposition method. In order to do this, the film and heterostructure contact line must remain stable on the surface for the approximately 30 minutes needed to complete the transfer to the silicon wafer, and then survive the transfer itself. During this time, the film is subjected to ambient air and water currents, as well as the induced water currents from the transfer itself, caused by removing subphase water from the trough. The successful transfer not only proves that edge-to-edge heterostructure films were created on the air-water interface, but also demonstrates their robustness and ability to be used once deposited. In short, the film stood up to a “real world” deposition technique. The ability to change materials in this way opens possibilities for heterojunction and other electronic devices to be entirely built floating on the air-water interface, and then transferred to other substrates including polymers, membranes, textiles, and biomaterials.

# Chapter 6
# Conclusion and Future Work

## 6.1 Summary of Findings

By studying the film formation of barrier free compressed Langmuir Blodgett films of 2D materials, we showed, for the first time, an edge-to-edge lateral heterostructure film free floating on the surface of water. This was accomplished by the careful study analysis of how these barrier-free, or spreading-compressed, films are formed, the critical parameters behind their formation. Furthermore, a mechanism was proposed for how these films are able to densify without any apparent force holding them in place, and how they can remain densified in a meta-stable way.

This understanding was enabled by the use of a developed video-based measurement technique, allowing for non-destructive in-situ characterization of the film. A seldom used image processing technique, videokymography, enabled the quick and easy processing of multiple hours of video into understandable images.

This characterization technique was then used to identify two modes of film deposition: jammed and flowing. It was shown that these modes exist for different materials and appear to be intrinsic to this deposition technique. The jammed mode was shown to contain a sharp increase in density once a critical amount of material was deposited on the surface, in contrast to the flowing mode, where film density increased linearly with material deposited. This observation was then expanded upon in the 3 phases of jammed film growth: gaseous, liquid, and solid. The sharp increase in density noted earlier was shown to be the transition from the gaseous film stage to the liquid film stage.

Analysis showed that the critical parameters to induce a jammed film were concentration, and the spreading ability of the dispersant mixture in which the nanomaterial is dispersed. It was shown that in the search space of spreading vs concentration, two distinct regions could be identified: jammed vs flowing, and these two regions can be easily separated. Within the flowing region, films deposit with a much lower final packing fraction, and a network like morphology, whereas in the jammed region, films deposit with a higher packing fraction and a cluster like morphology. These same features were seen using BAM imaging of the growing film. Experiments using inks with and without nanomaterial show that the addition of nanomaterial is critical to induce phase changes in the jamming regime.

This new understanding of film formation was then leveraged to create edge-to-edge lateral heterostructures on the air-water interface. Critical parameters of the deposition were identified: using material inks that deposit in the jamming regime, continuing the deposition to the point where the film was well into the solid phase (where it could withstand a disturbance in the interface), and choosing the material order such that the furthest spreading suspension was deposited first. The result was edge-to-edge heterostructure films with little to no mixing in the boundary layer between the two regions.

## 6.2 Recommendations for Future Work

### 6.2.1 Fluid Dynamic Analysis of the Spreading Front

In section 4.6, a mechanism was proposed for the rapid jamming transition from the gaseous to liquid phase. This mechanism relies on small vortices and fluid flow induced by spreading near the barriers of the deposition trough. While these vortices have been seen experimentally, a rigorous analysis of the fluid dynamics of the droplet spreading has not been done. Notably, much of the fluid flow of this system could be simplified to a 2D approximation, meaning analytical solutions to the Navier–Stokes equations become much more likely. This would add additional evidence for the proposed jamming mechanism and may even be able to show a theoretical order of the phase change.

### 6.2.2 Additional Heterostructure Materials

The edge-to-edge heterostructure presented here only consist of the materials rGO and $MoS_2$. These materials were chosen for their different ink dispersants, ability to be seen optically, and their common use in 2D material electronics (rGO being a stand-in for graphene). While the films presented serve as an excellent proof of concept, this technique of heterostructure films should be expanded to more materials, and individual films containing more than two materials. This would increase the relevance and applicability of this method. Notably, 2DLB films have been made using graphene oxide, electrochemically exfoliated graphene, and hexagonal-boron-nitride [11], [17], [45], [46]. These are all promising candidates.

### 6.2.3 Heterostructure Based Electronic Devices on the Air-Water Interface

As alluded to in the introduction, many of the 2D materials investigated in this thesis are electronically useful. The ability to create edge-to-edge heterostructures on the air-water interface

means that simple junctions can be created between two materials with little to no boundary mixing. These junctions form the basic unit for many electronic and optoelectronic devices. If more complex heterostructures, containing more materials, could be deposited on the air-water interface, it stands to reason that entire simple devices could be constructed on this interface. Aside from a novelty in itself, this would allow for easy device manufacturing and transfer to a verity of substrates.

# References


[1] D. Akinwande *et al.*, "A review on mechanics and mechanical properties of 2D materials—Graphene and beyond," *Extreme Mech Lett*, vol. 13, pp. 42–77, May 2017, doi: 10.1016/J.EML.2017.01.008.

[2] M. C. Lemme, D. Akinwande, C. Huyghebaert, and C. Stampfer, "COMMENT 2D materials for future heterogeneous electronics," 2007, doi: 10.1038/s41467-022-29001-4.

[3] P. Ajayan, P. Kim, and K. Banerjee, "Two-dimensional van der Waals materials," *Phys Today*, vol. 69, no. 9, pp. 38–44, Sep. 2016, doi: 10.1063/PT.3.3297.

[4] J. Y. Chong, B. Wang, and K. Li, "Water transport through graphene oxide membranes: the roles of driving forces," *Chemical Communications*, vol. 54, no. 20, pp. 2554–2557, Mar. 2018, doi: 10.1039/C7CC09120F.

[5] S. Stankovich *et al.*, "Graphene-based composite materials," *Nature 2006 442:7100*, vol. 442, no. 7100, pp. 282–286, Jul. 2006, doi: 10.1038/nature04969.

[6] P. Snapp, J. M. Kim, C. Cho, J. Leem, M. F. Haque, and S. W. Nam, "Interaction of 2D materials with liquids: wettability, electrochemical properties, friction, and emerging directions," *NPG Asia Materials 2020 12:1*, vol. 12, no. 1, pp. 1–16, Mar. 2020, doi: 10.1038/s41427-020-0203-1.

[7] W. Choi, N. Choudhary, G. H. Han, J. Park, D. Akinwande, and Y. H. Lee, "Recent development of two-dimensional transition metal dichalcogenides and their applications," *Materials Today*, vol. 20, no. 3, pp. 116–130, Apr. 2017, doi: 10.1016/J.MATTOD.2016.10.002.

[8] S. Yang *et al.*, "Emerging 2D Materials Produced via Electrochemistry," *Advanced Materials*, vol. 32, no. 10, p. 1907857, Mar. 2020, doi: 10.1002/ADMA.201907857.

[9] C. Huo, Z. Yan, X. Song, and H. Zeng, "2D materials via liquid exfoliation: a review on fabrication and applications," *Sci Bull (Beijing)*, vol. 60, no. 23, pp. 1994–2008, Dec. 2015, doi: 10.1007/S11434-015-0936-3.

[10] J. Wang *et al.*, “Rod-Coating: Towards Large-Area Fabrication of Uniform Reduced Graphene Oxide Films for Flexible Touch Screens,” *Advanced Materials*, vol. 24, no. 21, pp. 2874–2878, Jun. 2012, doi: 10.1002/ADMA.201200055.

[11] L. Xu, A. R. Tetreault, H. H. Khaligh, I. A. Goldthorpe, S. D. Wettig, and M. A. Pope, “Continuous Langmuir–Blodgett Deposition and Transfer by Controlled Edge-to-Edge Assembly of Floating 2D Materials,” *Langmuir*, vol. 35, no. 1, pp. 51–59, Jan. 2018, doi: 10.1021/ACS.LANGMUIR.8B03173.

[12] M. Bodik, M. Jergel, E. Majkova, and P. Siffalovic, “Langmuir films of low-dimensional nanomaterials,” *Adv Colloid Interface Sci*, vol. 283, p. 102239, Sep. 2020, doi: 10.1016/J.CIS.2020.102239.

[13] X. Li and J. F. Gilchrist, “Large-Area Nanoparticle Films by Continuous Automated Langmuir-Blodgett Assembly and Deposition,” *Langmuir*, vol. 32, no. 5, pp. 1220–1226, Feb. 2016, doi: 10.1021/ACS.LANGMUIR.5B03760/ASSET/IMAGES/ACS.LANGMUIR.5B03760.SOCIAL.JPEG_V03.

[14] A. Nasr Esfahani *et al.*, “Ultra-thin films of solution-exfoliated hexagonal boron nitride by Langmuir deposition,” *J Mater Chem C Mater*, vol. 8, no. 39, pp. 13695–13704, Oct. 2020, doi: 10.1039/D0TC02933E.

[15] Y. Zhang, L. Xu, W. R. Walker, C. M. Tittle, C. J. Backhouse, and M. A. Pope, “Langmuir films and uniform, large area, transparent coatings of chemically exfoliated MoS2 single layers,” *J Mater Chem C Mater*, vol. 5, no. 43, pp. 11275–11287, Nov. 2017, doi: 10.1039/C7TC02637D.

[16] Y. Zhang, L. Xu, W. R. Walker, C. M. Tittle, C. J. Backhouse, and M. A. Pope, “Langmuir films and uniform, large area, transparent coatings of chemically exfoliated MoS2 single layers,” *J Mater Chem C Mater*, vol. 5, no. 43, pp. 11275–11287, Nov. 2017, doi: 10.1039/C7TC02637D.

[17] A. Nasr Esfahani *et al.*, “Ultra-thin films of solution-exfoliated hexagonal boron nitride by Langmuir deposition,” *J Mater Chem C Mater*, vol. 8, no. 39, pp. 13695–13704, Oct. 2020, doi: 10.1039/D0TC02933E.

[18] H. Kaur, J. N. Coleman, H. Kaur, and J. N. Coleman, “Liquid-Phase Exfoliation of Nonlayered Non-Van-Der-Waals Crystals into Nanoplatelets,” *Advanced Materials*, vol. 34, no. 35, p. 2202164, Sep. 2022, doi: 10.1002/ADMA.202202164.

[19] A. V Tyurnina *et al.*, “Ultrasonic exfoliation of graphene in water: A key parameter study,” 2020, doi: 10.1016/j.carbon.2020.06.029.

[20] J. Chen, “Intrinsic Capacitance, Charge Storage Mechanisms, and Defect Engineering of Molybdenum Disulfide Nanosheets,” University of Waterloo, Waterloo, 2020. Accessed: Mar. 04, 2023. [Online]. Available: https://uwspace.uwaterloo.ca/handle/10012/15783

[21] M. Bodik, M. Jergel, E. Majkova, and P. Siffalovic, “Langmuir films of low-dimensional nanomaterials,” *Adv Colloid Interface Sci*, vol. 283, p. 102239, Sep. 2020, doi: 10.1016/J.CIS.2020.102239.

[22] M. M. Velázquez *et al.*, “Langmuir-Blodgett Methodology: A Versatile Technique to Build 2D Material Films,” *Two-dimensional Materials - Synthesis, Characterization and Potential Applications*, Aug. 2016, doi: 10.5772/63495.

[23] K. Y. C. Lee, “Collapse Mechanisms of Langmuir Monolayers,” *https://doi.org/10.1146/annurev.physchem.58.032806.104619*, vol. 59, pp. 771–791, Apr. 2008, doi: 10.1146/ANNUREV.PHYSCHEM.58.032806.104619.

[24] M. C. Larsen, “Binary phase diagrams at the air-water interface: An experiment for undergraduate physical chemistry students,” *J Chem Educ*, vol. 91, no. 4, pp. 597–601, Apr. 2014, doi: 10.1021/ED4004854/ASSET/IMAGES/MEDIUM/ED-2013-004854_0006.GIF.

[25] M. Bodik *et al.*, “Collapse Mechanism in Few-Layer MoS2 Langmuir Films,” *The Journal of Physical Chemistry C*, vol. 124, no. 29, pp. 15856–15861, Jul. 2020, doi: 10.1021/ACS.JPCC.0C02365.

[26] F. Arceri and E. I. Corwin, “Vibrational Properties of Hard and Soft Spheres Are Unified at Jamming,” *Phys Rev Lett*, vol. 124, no. 23, p. 238002, Jun. 2020, doi: 10.1103/PhysRevLett.124.238002.

[27] M. E. Cates, J. P. Wittmer, J.-P. Bouchaud, and P. Claudin, “Jamming, Force Chains, and Fragile Matter,” *Phys Rev Lett*, vol. 81, no. 9, p. 1841, Aug. 1998, doi: 10.1103/PhysRevLett.81.1841.

[28] A. J. Liu and S. R. Nagel, “Jamming is not just cool any more,” *Nature 1998 396:6706*, vol. 396, no. 6706, pp. 21–22, Nov. 1998, doi: 10.1038/23819.

[29] A. J. Liu and S. R. Nagel, “The Jamming Transition and the Marginally Jammed Solid,” *http://dx.doi.org/10.1146/annurev-conmatphys-070909-104045*, vol. 1, pp. 347–369, Jul. 2010, doi: 10.1146/ANNUREV-CONMATPHYS-070909-104045.

[30] C. S. O’Hern, L. E. Silbert, A. J. Liu, and S. R. Nagel, “Jamming at zero temperature and zero applied stress: The epitome of disorder,” *Phys Rev E*, vol. 68, no. 1, p. 011306, Jul. 2003, doi: 10.1103/PhysRevE.68.011306.

[31] V. Trappe, V. Prasad, L. Cipelletti, P. N. Segre, and D. A. Weitz, “Jamming phase diagram for attractive particles,” *Nature 2001 411:6839*, vol. 411, no. 6839, pp. 772–775, Jun. 2001, doi: 10.1038/35081021.

[32] D. J. Koeze and B. P. Tighe, “Sticky Matters: Jamming and Rigid Cluster Statistics with Attractive Particle Interactions,” *Phys Rev Lett*, vol. 121, no. 18, p. 188002, Nov. 2018, doi: 10.1103/PhysRevLett.121.188002.

[33] Y. Chai *et al.*, “Direct observation of nanoparticle-surfactant assembly and jamming at the water-oil interface,” *Sci Adv*, vol. 6, no. 48, Nov. 2020, doi: 10.1126/SCIADV.ABB8675.

[34] X. Ji, X. Wang, Y. Zhang, and D. Zang, “Interfacial viscoelasticity and jamming of colloidal particles at fluid–fluid interfaces: a review,” *Reports on Progress in Physics*, vol. 83, no. 12, p. 126601, Nov. 2020, doi: 10.1088/1361-6633/ABBCD8.

[35] D. F. Williams and J. C. Berg, “The aggregation of colloidal particles at the air—water interface,” *J Colloid Interface Sci*, vol. 152, no. 1, pp. 218–229, Aug. 1992, doi: 10.1016/0021-9797(92)90021-D.

[36] A. Kwan and A. M. Kwan, “‘Do Not Kill Guinea Pig before Setting up Apparatus’: The Kymograph’s Lost Educational Context,” *Teorie vědy / Theory of Science*, vol. 38, no. 3, pp. 301–335, Mar. 2017, doi: 10.46938/tv.2016.345.

[37] J. Švec, F. Sram, and H. K. Schutte, “Development and Application of Videokymography for High-Speed Examination of Vocal-Fold Vibration,” 2002.

[38] J. Chen, W. R. Walker, L. Xu, O. Krysiak, Z. She, and M. A. Pope, “Intrinsic Capacitance of Molybdenum Disulfide,” *ACS Nano*, vol. 14, p. 5648, 2020, doi: 10.1021/acsnano.9b10182.

[39] G. J. Silverberg *et al.*, “Controlling the Roughness of Langmuir–Blodgett Monolayers,” *Journal of Physical Chemistry B*, vol. 121, no. 19, pp. 5078–5085, May 2017, doi: 10.1021/ACS.JPCB.7B03549.

[40] NIMA Corporation, “ISR Flip | Characterization of thin films | KSV NIMA.” Accessed: Jun. 29, 2023. [Online]. Available: https://www.biolinscientific.com/ksvnima/characterization-of-thin-films/isr-flip

[41] J. G. Švec and H. K. Schutte, “Videokymography: High-speed line scanning of vocal fold vibration,” *Journal of Voice*, vol. 10, no. 2, pp. 201–205, Jan. 1996, doi: 10.1016/S0892-1997(96)80047-6.

[42] G. Lois, J. Blawzdziewicz, and C. S. O’Hern, “Jamming Transition and New Percolation Universality Classes in Particulate Systems with Attraction,” *Phys Rev Lett*, vol. 100, no. 2, p. 028001, Jan. 2008, doi: 10.1103/PhysRevLett.100.028001.

[43] W. Zheng, H. Liu, and N. Xu, “Shear-induced solidification of athermal systems with weak attraction,” *Phys Rev E*, vol. 94, no. 6, p. 062608, Dec. 2016, doi: 10.1103/PhysRevE.94.062608.

[44] X. Ji, X. Wang, Y. Zhang, and D. Zang, “Reports on Progress in Physics Interfacial viscoelasticity and jamming of colloidal particles at fluid-fluid interfaces: a review,” *Reports on Progress in Physics Rep. Prog. Phys*, vol. 83, p. 26, 2020, doi: 10.1088/1361-6633/abbcd8.

[45] L. Xu, M. Chekini, N. D. Wilson, R. J. Zamperoni, and M. A. Pope, “Spontaneous clustering of exfoliated two-dimensional materials at the air-water interface,” *J Colloid Interface Sci*, vol. 648, pp. 129–140, Oct. 2023, doi: 10.1016/J.JCIS.2023.05.157.

[46] M. Pahlevaninezhad *et al.*, “Exfoliated Graphene Composite Membrane for the All-Vanadium Redox Flow Battery,” 2023, doi: 10.1021/acsaem.3c00428.